Economic Geology, v. 118, no. 6, pp. 1467–1494

Diagenetic History and Timing of Cu and Zn-Pb Sulfide Mineralization in the Permian Kupferschiefer System, Saale Subbasin, Eastern Germany

Mohammed S. Mohammedyasin,[1,2,†] Joseph M. Magnall,[1] Sarah A. Gleeson,[1,2] Hans-Martin Schulz,[1] Anja M. Schleicher,[1] Jessica A. Stammeier,[1] and Bodo-Carlo Ehling[3]

[1]*Helmholtz Centre Potsdam GFZ German Research Centre for Geosciences, Telegrafenberg, Potsdam 14473, Germany*

[2]*Institute of Geological Sciences, Freie Universität Berlin, Malteserstrasse, 74-100, Berlin 12249, Germany*

[3]*Landesamt für Geologie und Bergwesen, Sachsen-Anhalt, Köthener Straße 38, D-06118 Halle, Germany*

Abstract

The Southern Permian basin in central Europe contains a number of important high-grade sediment-hosted Cu deposits. Laterally extensive stratabound Cu and Zn-Pb sulfide mineralized rocks are located at a major stratigraphic redox boundary, where coarse-grained continental sandstones of the uppermost Rotliegend Group are overlain by carbonaceous mudstones (T1) and limestones (Ca1) of the Zechstein Formation. This study investigates the diagenetic evolution and style of sulfide mineralization in three drill cores that intersect Cu and Zn-Pb sulfide mineralized rocks at three locations (Sangerhausen, Allstedt, and Wallendorf) in the Saale subbasin (Eastern Germany), which is located at the southern margin of the Southern Permian basin. We combine macro- to microscale petrographic data (binocular, transmitted and reflected light, and scanning electron microscopy) with quantitative X-ray diffractometry and bulk-rock geochemical analyses. Petrographic results show extensive, primary-porosity-occluding, early diagenetic calcite cementation that predates both the diagenetic alteration of detrital clasts and sulfide mineralization. The highest-grade Cu and Zn-Pb sulfides (bornite, sphalerite, and galena) replace the calcite cement, with subordinate replacement of dolomite and detrital clasts. Quantitative mineralogical and geochemical data demonstrate that the highest base metal (Cu, Zn, and Pb) concentrations are associated with carbonate-rich samples, mostly as disseminated mineralization in the middle T1. Bulk-rock geochemical results show enrichment and covariation of redox-sensitive trace elements (RSTEs, e.g., Mo) with total organic carbon content toward the lower T1, consistent with highly reducing depositional conditions. Overall, the distribution and dissolution of calcite cement across this stratigraphic redox boundary provided the main control on the lateral migration of base metal-bearing fluids and high-grade Cu and Zn-Pb sulfide mineralization in the Saale subbasin.

Introduction

Stratigraphic redox boundaries play a key role in the formation of a number of sediment-hosted stratiform to stratabound massive sulfide deposits (Hitzman et al., 2010). This is primarily because base metal (Cu, Pb, and Zn) solubilities are enhanced under oxidizing conditions and greatly lowered under reducing conditions (Seward and Barnes, 1997). The sediment-hosted stratiform Cu (SSC) deposits at the southern margin of the Southern Permian basin in Germany and Poland represent some of the world's most spectacular examples of sulfide mineralization associated with a stratigraphic redox boundary. This stratigraphic redox boundary is regionally extensive, extending from the United Kingdom to Poland, and records a transition from the terrestrially deposited Rotliegend sandstone (S1) to the organic-rich marine Kupferschiefer mudstone (T1). The T1 is overlain by the Zechstein limestone (Ca1). The highest Cu grades are in the T1, although sulfide-mineralized rocks are also found in the S1 and hanging-wall units of the lowermost Ca1 and overlying anhydrite unit (A1) (Borg et al., 2012).

Base metal-mineralized rocks in the Kupferschiefer (T1) and adjacent stratigraphic units are generally believed to have formed when slightly acidic, oxidizing, metal-bearing fluids encountered the redox boundary between the S1 and T1 and mixed with slightly alkaline, saline, and reduced sulfur-bearing pore fluids in the host rocks (e.g., Bechtel and Püttmann, 1991; Wedepohl and Rentzsch, 2006). One of the characteristic features associated with the high-grade ore is the "Rote Fäule," a term given to epigenetic hematitic alteration (e.g., Piestrzyński et al., 2002; Pieczonka et al., 2008; Borg et al., 2012). The Rote Fäule was initially interpreted to be an oxidized shallow-water facies that was equivalent to the reduced Cu-bearing T1, with the contrasting redox potentials reflecting the different sedimentary and diagenetic conditions (e.g., Franz, 1965; Jung and Knitzschke, 1976). However, subsequent studies have described the Rote Fäule as cross-cutting the stratigraphy, and the general consensus is that it has a postdepositional origin (Rydzewski, 1978; Oszczepalski, 1989).

Precise constraints on the timing of base metal sulfide formation in the Kupferschiefer district remain controversial. Several studies have suggested a syngenetic (e.g., Wedepohl, 1971) to early diagenetic (e.g., Wedepohl and Rentzsch, 2006) timing, i.e., base metal sulfides precipitated before major compaction and cementation. The preservation of negative $\delta^{34}S$ values (–40 to –25‰) in ore-stage sulfides has been used as evidence that reduced sulfur was generated via bacterial sulfate reduction (BSR) in an open system, during either syngenetic or early diagenetic mineralization (e.g., Sawlowicz, 1989). However, it has also been suggested that ore-stage

[†]Corresponding author: e-mail, moyasin@gfz-potsdam.de

ISSN 0361-0128; doi:10.5382/econgeo.5015; 28 p.
Digital appendices are available in the online Supplements section.

Submitted: August 18, 2022 / Accepted: February 14, 2023

sulfides could have replaced diagenetic pyrite and inherited the negative $\delta^{34}S$ values (Sun and Püttmann, 1997; Bechtel et al., 2001). Other studies have also proposed a late diagenetic timing of the mineralization, during tectonic hydrofracturing triggered by Triassic rifting (Jowett, 1986, 1987; Cathles et al., 1993). In these models, the reduced sulfur for the sulfide mineralization was derived from thermochemical sulfate reduction (TSR) (Heppenheimer et al., 1995; Sun and Püttmann, 2000). The preservation of higher $\delta^{34}S$ values (up to –8.4‰) in Cu sulfides from high-grade mineralized samples has also been linked with reduced sulfur derived via TSR at low temperatures (<130°C) during later diagenesis (Bechtel et al., 2001). These different models most likely reflect several stages of mineralization, from the diagenetic evolution of the Kupferschiefer in the late Permian to at least 100 m.y. after (Alderton et al., 2016).

The metal trap in sediment-hosted deposits may be influenced by a number of factors, including the depositional environment, diagenesis, and hydrothermal processes. In order to better understand how these different factors interact, it is necessary to generate different types of petrographic and geochemical data. For example, total organic carbon and bulk compositional data can be used to interpret the depositional redox conditions, which have a strong influence on organic matter preservation and sulfate reduction (Böning et al., 2012; Greenwood et al., 2013; Reinhard et al., 2014; Little et al., 2015; Magnall et al., 2018). Quantitative mineralogical data provide important constraints on the primary mineralogy of the host rocks, which is a first-order control on early (at near-surface, lower temperatures <50°C) and burial (higher depths and temperatures >50°–300°C) diagenetic processes (Morad et al., 2000). In fine-grained rock types, it may be necessary to combine standard petrographic techniques (transmitted and reflected light) with high-resolution scanning electron microscopy (SEM) to establish the relative timing (paragenesis) of diagenetic and hydrothermal mineral assemblages.

This study investigates samples from the S1, T1, and Ca1 in three drill cores (Sangerhausen, Allstedt, and Wallendorf) in the Saale subbasin (Eastern Germany). Different petrographic (transmitted and reflected light, SEM), mineralogical (quantitative X-ray diffraction [QXRD]) and geochemical (X-ray fluorescence [XRF] and inductively coupled plasma-mass spectrometry [ICP-MS]) data sets have been generated to investigate which aspects of the host rock determined the style of mineralization in the different units and localities. This requires consideration of (1) the evolution of paleoenvironmental conditions during the late Permian marine transgression, (2) how this influenced the diagenetic evolution of the S1, T1, and overlying Ca1, and (3) the relative timing and style of sulfide mineralization with respect to different diagenetic processes.

Geologic Background

Regional geodynamic and depositional setting of the Southern Permian basin

The Southern Permian basin is part of the intracontinental Central European basin system, which formed in the late Carboniferous to early Permian, contemporaneous with the assembly of the Pangea supercontinent (Plein, 1990; Ziegler, 1990; Fig. 1A). The crust beneath the Southern Permian basin comprises a complex assemblage of orogenic terranes that were accreted to Baltica and the East European craton during the Caledonian and Variscan orogenies (Ziegler, 1990). The varying crustal rheologies had an important role for stress and strain localization during the post-Variscan evolution of the Southern Permian basin (Maystrenko et al., 2008). The development of intracontinental basins during the latest Carboniferous-earliest Permian followed the end of the Variscan orogeny, coinciding with wrench faulting, thermal thinning of the lithosphere, and widespread magmatism (Ziegler, 1990; Wilson et al., 2004; Breitkreuz et al., 2008; Pharaoh et al., 2010).

The early Permian Rotliegend Group overlies the crystalline basement and Carboniferous (Westphalian-Stephanian) formations in the Southern Permian basin. Deposition of the Lower Rotliegend and Upper Rotliegend I was associated with bimodal volcanism in transtensive pull-apart basins (Stollhofen et al., 2008). The mafic and felsic volcanic rocks in the Lower Rotliegend are found in most parts of the Southern Permian basin but are particularly voluminous in the eastern part of the North German basin and Polish basin (Fig. 1A). The Upper Rotliegend II, comprising thick continental siliciclastics (~2,500 m thick) and evaporites, was influenced by tectonics and climatic fluctuations and also short-term marine ingressions (Legler and Schneider, 2008). It is dominated by ephemeral fluvial (wadi), sabkha, lacustrine, and aeolian successions (Stollhofen et al., 2008). Weissliegend and Grauliegend are used to describe local color variations in the uppermost part of the Upper Rotliegend II, which are composed of white to gray aeolian, fluvial, and locally marine sandstones (Ehling et al., 2008). The color variations are the result of chemical reduction during diagenesis, meaning the Weissliegend and Grauliegend are not strictly chronostratigraphic units (Borg et al., 2012).

During the late Wuchiapingian (Lopingian, ~258 Ma; Brauns et al., 2003), the Permian intracontinental basins were flooded by a marine transgression from the Boreal Ocean (Smith, 1979; Ziegler, 1990; Legler and Schneider, 2008). Besides the local occurrence of the so-called "Zechstein conglomerate" as a reworked horizon and a basal carbonate layer, the marine transgression resulted in the deposition of the T1, Ca1, and Werra anhydrite (A1) of the Werra Formation (Fig. 1B, C). The T1 is composed of three subunits, where organic matter is highest in the lower T1 (T1-L) and carbonate increases upward into the middle and upper T1(T1-M and T1-U) (Grice et al., 1997). The T1 has been dated at 257.3 ± 1.6 Ma using the Re-Os system (Brauns et al., 2003), meaning deposition during the Wuchiapingian (Lopingian). This is supported by the depositional age (258 Ma) for the top of the underlying Elbe Group (Menning et al., 2006). This age is generally in agreement with a less precise Re-Os isochron age of 247 ± 20 Ma of Pašava et al. (2010) for unmineralized T1 samples from the Zdrada area in northern Poland. These ages also overlap with K-Ar ages of 277 to 249 Ma for authigenic illite from unmineralized T1 samples in northwest Poland (Bechtel et al., 1999).

Geology of the Saale subbasin

The SW-NE–trending Saale subbasin is approximately 150 × 90 km and located to the southeast of the Harz mountains

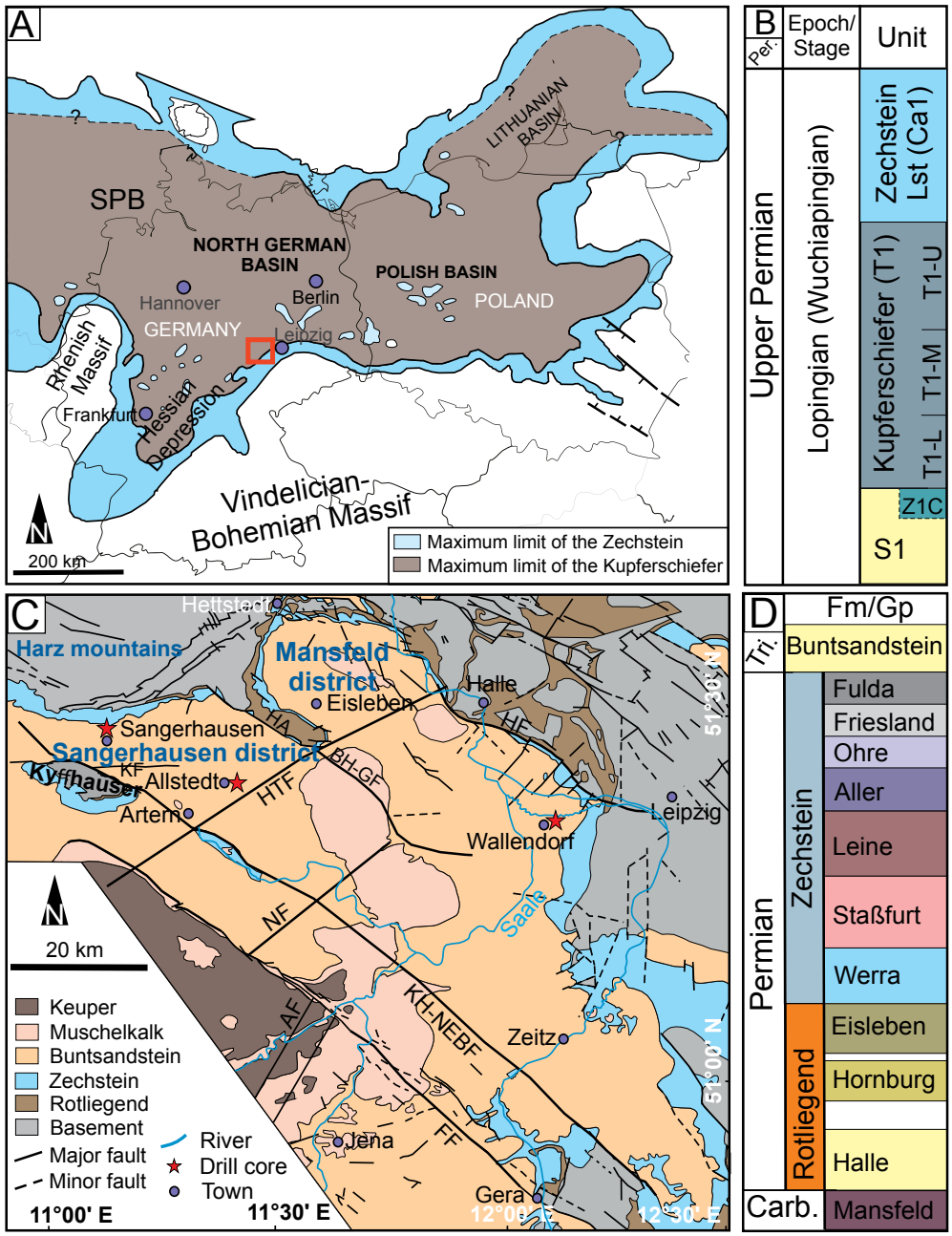

Fig. 1. (A) A map showing the extent of the Kupferschiefer and Zechstein in the Southern Permian basin (SPB) (Erzberger et al., 1968; Kulick et al., 1984; Paul, 2006). The red square shows the approximate location of the Saale subbasin. (B) Generalized stratigraphy of the Kupferschiefer system in the Southern Permian basin consisting of the uppermost Rotliegend sandstone (S1), Kupferschiefer (T1), and Zechstein limestone (Ca1) (Stollhofen et al., 2008; Ruebsam et al., 2017). (C) Geologic map of the Saale subbasin (modified from Geologisches Landesamt Sachsen-Anhalt, 1993). The northern and eastern limits of the Saale subbasin are defined by crystalline basement rocks and the southwestern limit by the Thuringian subbasin (not shown). (D) Simplified Permian stratigraphy of the Saale subbasin. AF = Apolda fault, BH-GF = Blankenheim-Geiseltal fault, FF = Finne fault, Fm = Formation, Gp = Group, HA = Hornburger anticline, HF = Halle fault, HTF = Hornburger-Tiefen fault, KF = Kelbra fault, KH = Kyffhäuser, KH-NEBF = Kyffhäuser NE-Boundary fault, NF = Nebra fault, Z1C = Zechstein conglomerate.

and northeast of the Thuringian subbasin (Fig. 1C). The crystalline basement is overlain by Visean to Westphalian sedimentary rocks (Schneider and Romer, 2010). The Stephanian Mansfeld Group is composed of (1) the basal fine-grained coal-bearing sedimentary rocks of the Grillenberg subformation and coarse-grained sedimentary rocks of the Gorenzen Formation, (2) unconformably overlying thick red beds of the Rothenburg Formation, and (3) braided river deposits of the Siebigerode Formation (Schneider et al., 1995; Schneider and Romer, 2010; Gebhardt and Hiete, 2013).

The overlying early Permian Rotliegend Group, cropping out in most marginal parts of the Saale subbasin, comprises

chert-quartzite-conglomerates interbedded with lacustrine black shales of the Halle Formation with silica-rich volcanic rocks as sills and laccoliths (Fig. 1D). The Halle Formation is overlain by medium- to coarse-grained sandstones of the Hornburg Formation and braided river sandstones of the Eisleben Formation (Ehling et al., 2008). The T1 in the Saale subbasin is a thin (0.3–0.6 m), organic matter-rich mudstone unit and was historically mined for copper and other metals in the Sangerhausen and Mansfeld mining districts. The different districts in the Saale subbasin are separated by structural highs (e.g., Hornburger anticline) and major faults (e.g., Hornburg-Tiefen fault) (Fig. 1C). In addition, the Saale subbasin has also been affected by several northwest-southeast minor faults.

Base metal mineralization of the Kupferschiefer system in Germany and Poland

The Kupferschiefer system in Germany and Poland hosts the world's second-largest SSC district, with combined resources of >60 Mt of contained copper (Borg et al., 2012). Copper and associated metals have historically been mined in different mining districts and are being actively mined in the Sieroszowice, Rudna, and Lubin districts in Poland (Oszczepalski et al., 2019).

The sulfide mineralization in the Kupferschiefer system is laterally extensive in the S1, T1, and Ca1 and is found locally in the Werra anhydrite A1. Different styles of sulfide mineralization have been described, including disseminated, vein-type, and detrital clast and fossil replacement sulfides (see summary by Borg et al., 2012). Metal zonation has been described as having a lateral component in the German Kupferschiefer districts and an oblique vertical component in the Polish Kupferschiefer districts (Borg et al., 2012). In either case, the zonation is characterized by (1) a Cu zone, adjacent to the Rote Fäule alteration, comprising chalcocite, bornite, chalcopyrite, and some other minor Cu sulfides, (2) an overlapping Zn-Pb zone, and (3) a noneconomic pyrite zone (Borg et al., 2012). The principal sources of copper in the Kupferschiefer system are unknown, but could be either the mafic volcanic rocks in the Rotliegend or the basement rocks of the Mid-European Crystalline High (Borg et al., 2012). Lead isotope data of galena ± sphalerite ± pyrite ores and vein galena from different parts of the Southern Permian basin suggest the basement rocks are a major source of Pb for the mineralization (Wedepohl et al., 1978).

In terms of geochronology, indirect paleomagnetic age data of hematite in the Polish basin suggest a Triassic age (250–220 Ma) of the Rote Fäule (Jowett et al., 1987). This paleomagnetic age is bracketed by the K-Ar ages of illites (~250 Ma) in mineralized samples close to the Rote Fäule (Bechtel et al., 1996) and by the estimated age of diagenetic illite (216–190 Ma) in the mineralized T1 samples in the Polish basin (Bechtel et al., 1999). A range of Re-Os ages have been derived for mineralized samples from the Polish basin, which correspond with different mineralization styles (Alderton et al., 2016). The Re-Os ages indicate that the fine-grained sandstone infill and massive ore that formed during the late Permian-Early Triassic and younger ages (Early to Middle Jurassic) correspond with sulfide veinlets. The paleomagnetic age data of hematite in the Rote Fäule in the Sangerhausen mining district (Eastern Germany) also suggest two distinct ages (Symons et al., 2011): 149 ± 3 Ma (Late Jurassic), which probably represent the disseminated, high-grade, Cu-Zn-Pb mineralization, and 53 ± 3 Ma (early Eocene) for the vein mineralization (Borg, 2017). The age discrepancy in the two basins could be related to either a local, younger postdiagenetic mineralizing event, such as structurally controlled (Rücken-type veins) mineralization associated with Carpathian-Alpine tectonism characterized by the presence of cobalt, nickel, and silver arsenide minerals (Wagner and Lorenz, 2002; Zientek et al., 2015) or a local fluid-flow event unrelated to the Cu-mineralizing system (e.g., Wilkinson et al., 2017).

Methods

Sampling

Samples were selected from three different drill cores in the Saale subbasin (Eastern Germany; Figs. 1C, 2). Drilling took place in the 1980s for mineral exploration. The samples were selected from the Sangerhausen 102/80 (depth: 429.6–430.6 m), Allstedt 11/86 (depth: 945.4–946.4 m), and Wallendorf/Luppe 6/84 (depth: 359.1–360.1 m) drill holes. Each drill core contains the uppermost part of the Rotliegend sandstone (S1), Kupferschiefer (T1), and lowermost Zechstein limestone (Ca1) (Fig. 2A-C). These drill holes also intersect different sulfide zones: the Sangerhausen (SHN) drill hole intersects the Rote Fäule and Cu zone, the Allstedt (AST) drill hole intersects the Cu zone and overlapping Zn-Pb zone, and the Wallendorf (WDF) drill hole intersects the Zn-Pb zone (Fig. 2A-C). A total of 47 samples (SHN =17, AST = 17, and WDF = 13) were collected from the three drill cores, each every ~5-cm interval. The samples were split, with one-half prepared into polished thin and thick sections, and the other half powdered for mineralogical and geochemical analyses.

Petrography

All analyses were carried out at the German Research Centre for Geosciences (GFZ-Potsdam). Hand sample photographs and binocular microscope images were taken to inspect variations in lithology, mineralogy, and organic matter. Standard polished thin sections (~25-mm thickness) and polished thick sections (~2-mm thickness) were prepared for petrography for all samples. Transmitted- and reflected-light petrography was performed on a BX51 polarizing microscope (Olympus Corporation). Organic petrography was performed on a DM4 P microscope (Leica) under an oil immersion objective lens using ultraviolet (UV) light and reflected white light illumination. Backscattered electron (BSE) and secondary electron (SE) imaging together with electron dispersive spectrometry (EDS) semiquantitative compositional analysis was performed using an Ultra Plus field emission scanning electron microscope (Carl Zeiss Microscopy GmbH). The EDS analysis was conducted using an accelerating voltage of 20 kV. False-color elemental composite maps were generated to determine the distribution of the different mineral phases.

Quantitative mineralogy

Mineralogical and geochemical analyses (except total carbon and total organic carbon content) were performed at the Elements and Minerals of the Earth Laboratory (ElMiE-Lab) at

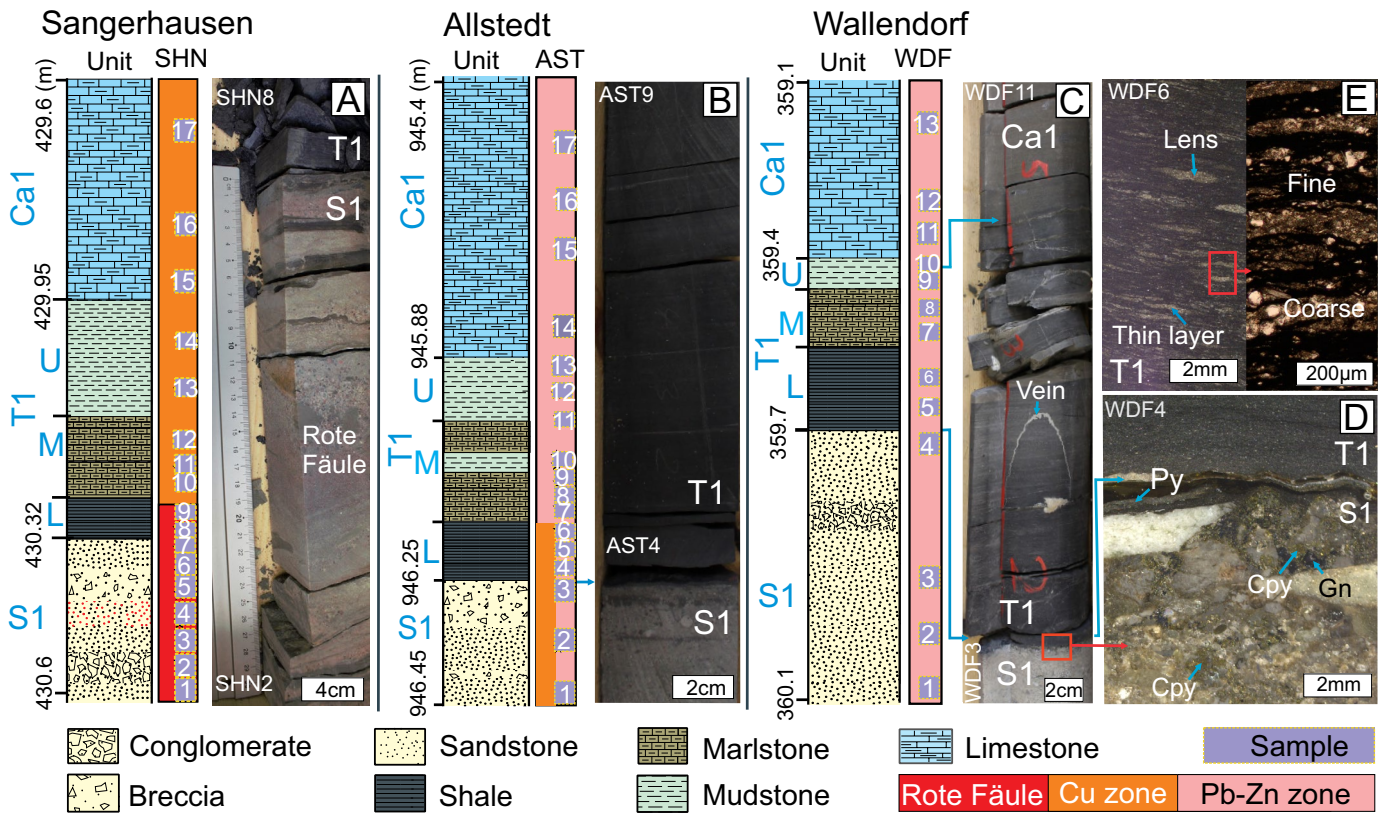

Fig. 2. Stratigraphic and lithological logs and selected sample photographs for the three drill cores from Sangerhausen (SHN), Allstedt (AST), and Wallendorf (WDF) localities. The sampled intervals are annotated numerically alongside each graphical log. (A) Drill core photograph (430.32–430.55 m) showing the contact between the Rote Fäule alteration in the S1 and the overlying carbonaceous mudstone (T1). (B) Drill core photograph (946.07–946.25 m) showing the contact between the S1 and T1. (C) Drill core photograph (359.35–359.68 m) showing the S1, T1, and Ca1. (D) Binocular microscope image of the S1 sample (WDF4) showing galena, sphalerite, and chalcopyrite replacing detrital clasts and filling intergranular pores. (E) Binocular microscope photograph and transmitted-light photomicrograph (WDF6) showing an overview of fine- and coarse-grained laminations in the lower T1 (T1-L). Cpy = chalcopyrite, Gn = galena, Py = pyrite.

GFZ-Potsdam. Forty-seven bulk-rock samples were crushed and powdered to a grain size of <62 µm. For quantitative mineral analysis, the powdered samples were further milled to a grain size of <10 µm using a micronizing mill (McCrone Group). Analyses were performed with an X-ray diffractometer (Malvern PANalytical) using a Bragg-Brentano geometry at 40 mA and 40 kV with CuKa radiation, and a PIXel3D detector at a step size of 0.013° 2θ from 4.6° to 85° 2θ and 60 s per step. The mineralogy was determined with the software EVA (version 11.0.0.3) by Bruker using an updated mineral library. Rietveld refinement for quantitative mineralogy was performed using the program BGMN (Bergmann et al., 1998) and the open-source software package Profex (version 4.3; Doebelin and Kleeberg, 2015), calibrated for the used diffractometer. The error is in the range of 3%.

Bulk-rock geochemistry

Major and minor elements were determined on glass beads on <62-µm powdered sample split and analyzed by XRF using an Axios Advanced spectrometer (Malvern PANalytical). The quantification level was 0.02 wt % for major elements and 10 ppm for minor elements. Loss on ignition (LOI) was measured as weight loss during the ignition of the sample. Total S was measured by the Eltra elemental analyzer (Eltra CS 2000). For trace element analysis, samples were digested using the standard four-acid digestion method (concentrated AR/HF/$HClO_4$) using closed Savillex beakers on a hot plate at 180°C. After 24 h, the samples were checked for undissolved residue and evaporated to dryness. The digestion procedure was repeated until no residue was visible. Dissolved samples were diluted in 2 vol % HNO_3. All acids were prepared using reagents purified by subboiling distillation and diluted by bidistilled H_2O. Acid blanks of concentrated reagents are routinely tested. Trace elements were analyzed by high-resolution (HR-)ICP-MS using an Elements XR instrument (Thermo Fisher). Drift correction was performed by internal standard and addition of 1 µg/kg In. One procedural blank was included per 18 samples and was generally negligible compared to sample concentrations. Acid blanks are subtracted online. Measurements were repeated two to four times with repeatability generally within 5%.

The total carbon and total organic carbon contents were analyzed with an elemental analyzer (EA Isolink IRMS system, Thermo Fisher). For total carbon determination, about 5 mg of sample material was loaded into Sn capsules and burned in the elemental analyzer. Total organic carbon content was determined on in situ decalcified samples (3 mg). To remove the carbonate carbon, samples were loaded in Ag capsules and

decalcified in two rounds by 3% HCl and 20% HCl, respectively, and heated for 3 h at 75°C. Both measurements were calibrated against urea and checked with an internal laboratory standard (TSK). The reproducibility for replicate analyses for total carbon and total organic carbon was better than 0.2 wt %.

Results

Petrography

The relative timing of the different mineral phases formed in each of the major units is presented in a paragenetic chart in Figure 3, and key paragenetic relationships are described below.

Rotliegend sandstones (S1): The analyzed samples comprise fine- to coarse-grained, poorly to moderately sorted, rounded to subrounded and randomly oriented detrital clasts composed of mostly submillimeter-size grains of quartz, feldspar, and lithic/rock fragments (Fig. 4A, B; App. Fig. A1A-D). Some larger (cm size) clasts have been preserved in the Sangerhausen drill core. Monocrystalline quartz clasts dominate over polycrystalline quartz (App. Fig. A1A). Plagioclase (albite) and K-feldspar mainly compose the detrital feldspar fraction. Rock fragments commonly have source-specific textures and compositions that can be used to identify them in thin sections (Ulmer-Scholle et al., 2015). Accordingly, the rock fragments include both felsic and mafic igneous, sedimentary, metasedimentary, and metamorphic rock fragments (App. Fig. A1A-D). The mafic rock fragments are mostly composed of quartz and albite where their groundmasses altered to, or were replaced by, early illite and chlorite (e.g., Fig. 4C, D).

Diagenetic assemblages in the sandstones include carbonate (calcite and minor dolomite) and sulfate (anhydrite and trace barite) cements, and clays (illite, chlorite, and kaolinite) (Figs. 4–6). The carbonate cement in the sandstones occurs as extensive, poikilotopic, intergranular calcite cement that forms overgrowths on minor rhombic dolomite (~5–10 μm) and also ingresses into intragranular pores (Fig. 4D-H). In samples from the Sangerhausen drill core, the calcite cement is zoned, and certain domains contain bladed hematite (Figs. 4F, H, 5B), producing the red color at hand-specimen scale (Fig. 2A). The hematite intergrowth mostly occurs in the outer parts of the intergranular calcite cement (Figs. 4F, H, 5B, C) but is also present as overgrowths on euhedral dolomite (Fig. 5C). The intergranular pore-filling calcite shows dissolution textures in all drill cores (Fig. 5B, C). These sandstones also contain poikilotopic anhydrite and trace barite cements (Figs. 4E, F; App. Fig. A2D). Anhydrite cement is mostly cogenetic with calcite cement and is more abundant in the Sangerhausen than in the Allstedt and Wallendorf drill core samples (Fig. 4E, F).

Mafic volcanic rock fragments have been cemented by calcite (± anhydrite), and their groundmasses are altered to or replaced by illite and chlorite (Figs. 4B-D; App. Fig. A2A, B). These altered clasts sometimes have serrated edges that allow inward growth of intergranular calcite cement (Fig. 4C). This interlayered illite with minor chlorite also occurs rarely in the intergranular pores (e.g., Fig. 5C). Rounded detrital albite clasts have been also replaced by calcite and minor anhydrite (± barite) cement intergrown with kaolinite (Fig. 5D, E). Kaolinite is only preserved in these assemblages in the intragranular pores (Fig. 5E, F). Detrital feldspar and quartz clasts have grain boundaries that are etched and corroded, and the released ions precipitated to intergranular late, meshwork illite (Fig. 4H; App. Fig. A2C), probably after the dissolution of intergranular calcite cement (Fig. 5B).

The sulfides in the sandstones include (1) accessory bornite and covellite in the Sangerhausen samples (Fig. 4F), (2) bornite and sphalerite in the Allstedt samples (Fig. 6A-F; App. Fig. A2F), and (3) galena and sphalerite with minor chalcopyrite and enargite in the Wallendorf drill core samples (Fig. 6G, H; App. Fig. A2G, H). These sulfides occur predominantly as a replacement of intergranular calcite cement, but also of detrital clasts (Fig. 6A-H; App. Fig. A2E-H). For example, the sulfides may have replaced clasts that have been first replaced by calcite (e.g., Fig. 6C). This is consistent with numerous examples of clasts that have been replaced by calcite (Figs. 4E, 5A, B). No pyrite was observed in the sandstones.

Kupferschiefer (T1): The T1 is composed of shale (lower T1 [T1-L]), carbonate-rich marlstone/mudstone (middle T1 [T1-M]), and mudstone (upper T1 [T1-U]) (Fig. 2A-C). The framework grains in these subunits are mainly clasts of quartz and albite. The matrix is composed of clay minerals, mainly illite and minor chlorite and kaolinite. The lower T1 contains alternating coarse and fine-grained laminations (Figs. 7A-C, 8A-H). The coarser-grained laminations are composed of detrital clasts of quartz (~50 μm) and albite (~30 μm), whereas the fine-grained laminations are dominated by organic matter-rich layers of illite ± chlorite ± kaolinite (Figs. 7A-C, 8A-H). The middle and upper T1 are composed of quartz and albite, cemented by calcite, dolomite, and minor anhydrite (Fig. 9A, B).

Organic petrographic and reflected UV and white (RW) light investigations of samples from the Sangerhausen and Wallendorf drill cores showed different macerals in the T1. These include vitrinite-like macerals, alginite, and inertinite (Fig. 7A, B). Vitrinite-like macerals are very thin (<10 μm) and conformable with clay laminations. They are abundant in the lower T1 in both drill cores (Fig. 7A, B). Framboidal pyrite (~5 μm) is mostly associated with these vitrinite-like macerals and is generally ubiquitous in clay-rich layers (Fig. 7A, B). Alginite with greenish-yellow fluorescent colors is partially degraded in the Sangerhausen drill core samples and better preserved in the Wallendorf drill core samples (Fig. 7C-E). Carbonates have a very high fluorescence and are mostly associated with sulfides both in the T1 and Ca1 (Fig. 7C-E).

Diagenetic assemblages in the T1 include carbonate (calcite and dolomite) and sulfate (anhydrite) cements and illite (Figs. 8A-H, 9A-E). In the lower T1, there is greater dolomite and less calcite cement in the coarser-grained laminations (Fig. 8A, B). In the middle and upper T1, fine-grained calcite (5–20 μm) forms a cement to euhedral to subrounded dolomite (~5 μm) and framework grains. The abundant calcite cement has occluded intergranular pores and is most abundant in the middle T1 (Fig. 9A-C). Trace anhydrite cement is also preserved as intergranular cement (Fig. 9A).

Carbonate cements and feldspars (albite and K-feldspar) have been affected by partial to complete dissolution in the T1, especially in the coarse-grained laminations in the lower T1 (Fig. 8C-F). In the middle and upper T1, calcite cement

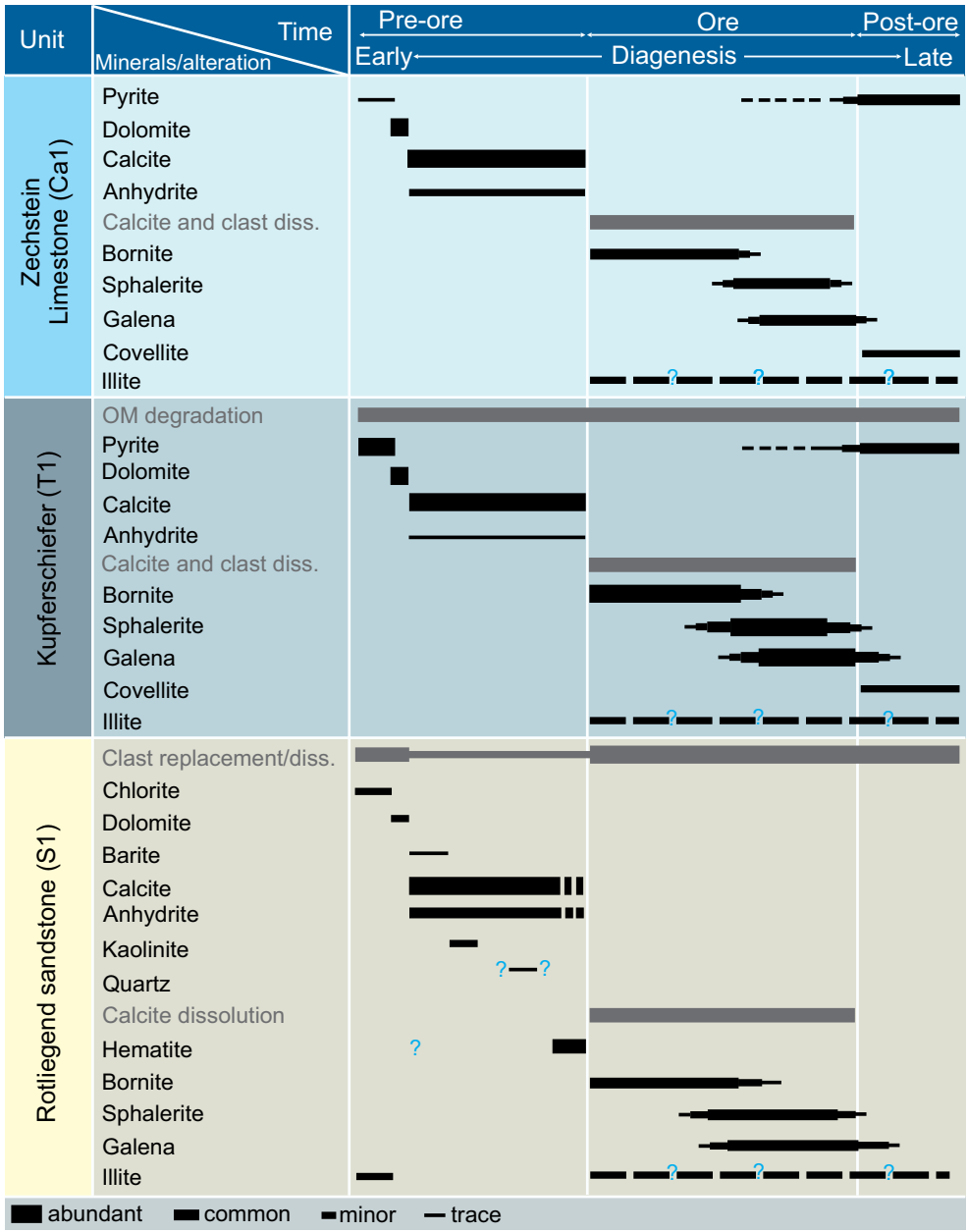

Fig. 3. A paragenetic chart for the mineral phases in the Rotliegend sandstone (S1), Kupferschiefer (T1), and Zechstein limestone (Ca1). diss = dissolution, OM = organic matter.

has been significantly affected by dissolution relative to albite and dolomite (Fig. 9A, B).

Framboidal pyrite is ubiquitous in the T1, especially in the fine-grained laminations in the lower T1 and foraminiferal tests at the boundary between the T1 and Ca1 (App. Fig. A3A-C). The ore-stage sulfides in the T1 have a style of replacement similar to that in the S1. In the lower T1, sulfides replace calcite and dolomite (e.g., bornite in the Sangerhausen, bornite and sphalerite in the Allstedt, and sphalerite and galena in the Wallendorf drill core samples) and, to a lesser degree, detrital clasts in coarse-grained laminations (Fig. 8C-F; App. Fig. A3E, F). In the middle T1 with high-grade Cu and Zn-Pb sulfide assemblages, the sulfides clearly replace the calcite cement (Fig. 9A-E). The post-ore-stage mineralization occurs parallel to bedding or as disseminated pyrite in T1 (e.g., App. Fig. A3D), but the abundance increases upward in each drill core. Furthermore, sphalerite and pyrite (not shown) occur in crosscutting calcite veins mostly in the Wallendorf drill core in the middle T1 (Fig. 9F). The sulfide assemblages in the middle T1 extend to the upper T1 though the type and abundance of sulfides may vary in different drill cores.

Zechstein limestone (Ca1): The Ca1 is largely composed of dolomite and a significant amount of quartz and phyllosilicates (illite and minor chlorite ± kaolinite) (Fig. 10A, B). Both euhedral and subhedral to anhedral (circular) dolomite (~5 μm) have been observed in the Ca1. The dominant intergranular cement in the Ca1 is highly fine grained calcite

cement (<5 μm) with minor Fe oxide and anhydrite (Fig. 10A-C). The vuggy pores in calcite cemented dolomite are aligned in specific directions in hand-specimen (cm) scale and mostly filled with illite or sulfides (Figs. 7F, 10C, E). The sulfides in the Ca1, similar to the upper T1, include bornite, covellite, and post-ore-stage pyrite in the Sangerhausen drill core and sphalerite, galena, and post-ore-stage pyrite in the Allstedt and Wallendorf drill cores (e.g., Fig. 10D-F). The edges of bornite grains are altered to covellite in the Sangerhausen drill core samples (Fig. 10D).

Quantitative mineralogy

Quantitative mineralogical data for the samples from the Sangerhausen, Allstedt, and Wallendorf drill cores are available in a supplementary data file (Mohammedyasin et al., 2022) and summarized in Figure 11A through C. Major mineral phases in the S1, T1, and Ca1 include quartz, plagioclase, K-feldspar, calcite, dolomite, phyllosilicates (muscovite, phlogopite, illite, and chlorite), and pyrite (Fig. 11A-C). Some of the minor to accessory minerals (<1%) confirmed in SEM analysis include biotite, anhydrite, barite, hematite, and Ti dioxide (rutile). The samples have been classified on the basis of quartz + feldspar, phyllosilicate, and carbonate content and subdivided according to lithological units (Fig. 12). The previous sedimentological classification of the T1 into three—T1-I (shale), T1-II (claystone), and T1-III (marlstone)—was generally based on assumptions that carbonate content increases upward. However, the carbonate in the T1 is an early diagenetic phase (i.e., is not primary) and is higher in the middle T1 than in the upper T1 in the drill cores. Hence, we reclassify the T1 mineralogically into three subunits: lower T1 (T1-L, shale), middle T1 (T1-M, mudstone to marlstone), and upper T1 (T1-U, mudstone) (Fig. 12). The QXRD data of the T1 samples from this study are in a good agreement with the T1 samples from the Mansfeld, Wettelrode, Polkowice, Rudna, and Lubin Kupferschiefer districts (Rahfeld et al., 2018; Fig. 12).

The quartz and feldspar content in the S1 samples is slightly lower in the Sangerhausen (mean = 57%) than in the Allstedt (73%) and Wallendorf (68%) drill cores (Fig. 11A-C), whereas the carbonate content in the Wallendorf samples (10%) is lower than in the Sangerhausen (21%) and Allstedt (18%) samples. The phyllosilicate content in the Allstedt samples (8%) is lower than in the Sangerhausen (21%) and Wallendorf (22%) samples. Minor bornite and accessory sphalerite were observed in the S1 samples (AST3 and WDF4) adjacent to the T1 from the Allstedt and Wallendorf drill cores. Furthermore, rare anhydrite occurs only in the Sangerhausen samples (max. 3%).

Samples from the lower T1 contain higher phyllosilicate (mean = 46%) and lower carbonate (12%) contents. The quartz + feldspar and phyllosilicate contents in the middle (T1-M, 31%, 31%) and upper (T1-U, 32%, 33%) T1, respectively, are generally proportional. However, the total carbonate content is slightly higher in the middle T1 (32%) than in the upper T1 (27%). There is a notable difference in carbonate mineralogy (calcite and dolomite) between drill cores. In samples from the Sangerhausen and Allstedt, calcite is dominant in the S1 and dolomite increases upward into the T1 (Fig. 11A, B; App. Fig. A4A, B). In contrast, in samples from the Wallendorf drill core, calcite is the dominant carbonate phase throughout the S1 and T1 (Fig. 11C; App. Fig. A4C). Sphalerite was quantified in the Allstedt and Wallendorf drill core samples, and bornite (AST6) and galena (WDF6 and WDF10) only in a few Allstedt and Wallendorf drill core samples. Pyrite is abundant in the lower and upper T1 in all drill cores (Fig. 11A-C; App. Fig. A4A-C). Samples from the Ca1 comprise high quartz, feldspar, and phyllosilicate contents (combined mean ~50%), which are proportional to carbonates.

Bulk-rock geochemistry

The bulk-rock major and trace element composition of all samples from the Sangerhausen, Allstedt, and Wallendorf drill cores is available in a supplementary data file (Mohammedyasin et al., 2022).

Trends in major elements and base metal composition in the Rotliegend sandstone (S1): The SiO_2 concentration is slightly lower in the Sangerhausen (range = 50–65.5 wt %, mean =

Fig. 4. Backscattered electron (BSE) images of key samples. The name of the drill core (AST = Allstedt, SHN = Sangerhausen, WDF = Wallendorf) is written on each image, in this figure and hereafter. (A) Sample AST3 showing poorly sorted detrital clasts (Qz = quartz; dark gray) with intergranular pore space cemented by calcite (Cal; light gray). The red arrows highlight the grain boundary of a clast composed of detrital quartz and albite (Ab) where the groundmass has been altered to illite (Ilt) and chlorite (Chl) and replaced by calcite cement. The red and yellow arrows in the upper right-hand corner highlight detrital albite partially replaced by K-feldspar. (B) A mixture of clast types and sizes cemented by calcite. Mafic volcanic clasts have been strongly altered to illite and chlorite, and bornite (Bn) has partially replaced the calcite cement. The serrated dissolution contact (green arrow) between an altered mafic rock fragment and the calcite cement suggests acidity generated during clast alteration resulted in calcite dissolution (sample AST3). The red arrows highlight the grain boundary of an altered volcanic rock fragment. (C) A BSE image showing the complex intergrowth of illite, chlorite, and quartz in a highly altered mafic rock fragment (sample AST3). (D) A BSE image of sample SHN4 showing a mixture of clast types in an intergranular calcite cement. A clast of detrital albite has been partly altered to kaolinite (Kln), and replaced by calcite, anhydrite (Anh), and barite (Brt). The red arrows highlight the grain boundary of an altered volcanic rock fragment. (E) A BSE image showing a small clast that has been completely replaced by calcite and anhydrite. The altered clast has then been partially replaced by bornite. The calcite cement has multiple growth zones and overgrows an earlier generation of minor dolomite (Dol) rhombs. Small crystals of bladed hematite (Hem) are intergrown with a latest stage of the calcite cement (sample SHN4). The calcite cement also ingressed into intragranular (IntraG) pores (upper-left corner). The orange arrows show dissolution of detrital quartz. (F) A high-resolution BSE image showing complex growth zoning in the calcite (planar crystal boundaries are denoted by yellow arrows). One of the calcite growth zones is intergrown with bladed hematite (sample SHN4). (G) A BSE image showing a strongly altered clast, where the inset image shows an assemblage of illite and chlorite. The other subrounded clasts are primarily quartz and cemented by calcite (sample SHN4). (H) A BSE image showing complex growth zones (yellow arrow) in the calcite cement, including a domain that has been partially replaced by bladed hematite. Small dolomite rhombs have also been overgrown by calcite, which contains minor inclusions of hematite (sample SHN4). Ti-ox = titanium oxide.

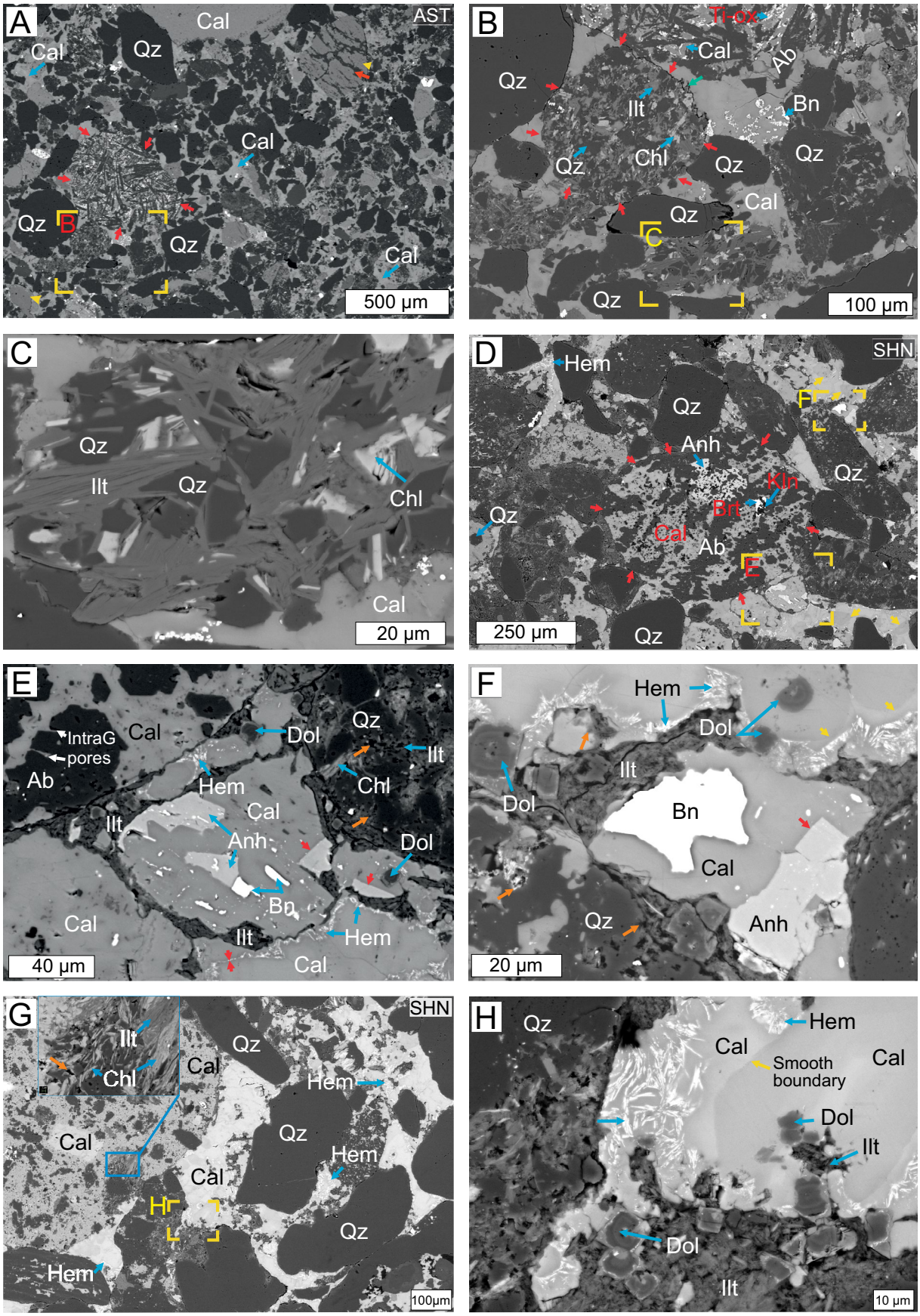

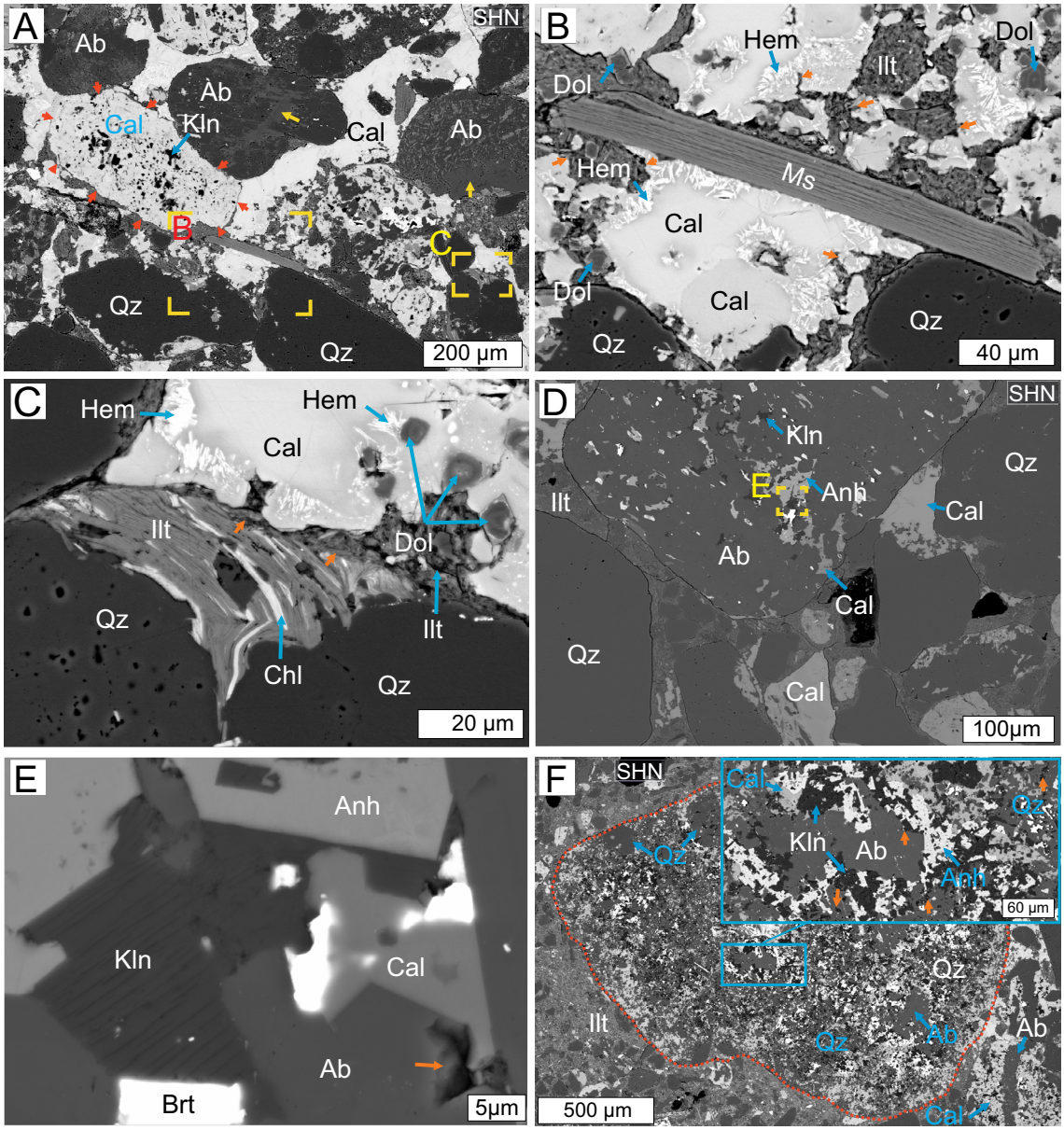

Fig. 5. (A) A mixture of clast types cemented by poikilotopic calcite. The clast highlighted by red arrows has been almost completely replaced by an assemblage of calcite and kaolinite. Clasts of albite (Ab) have been partially altered to K-feldspar (yellow arrow) (sample SHN4). (B) Zoned calcite (Cal) cement with bladed hematite (Hem) microcrystals and fine-grained illite (Ilt) matrix. The preservation of the undeformed muscovite (Ms) crystal indicates cementation happened before major compaction (sample SHN4). (C) Illite and chlorite (Chl) crystals rimming two quartz (Qz) clasts. The cement is zoned calcite, which has overgrown microcrystals of rhombic dolomite. Bladed hematite is intergrown with the final stage of calcite cement (sample SHN4). (D) Rounded detrital clasts cemented and partially altered by calcite. The large albite clast has been partially altered by kaolinite (Kln) and anhydrite (Anh) (sample SHN4). (E) A high-resolution backscattered electron (BSE) image showing an intergrowth of albite, calcite, anhydrite, kaolinite, and barite (Brt) (sample SHN4). (F) A large detrital clast composed of quartz and albite (highlighted by a red dotted line) replaced by calcite and anhydrite, which are intergrown with kaolinite (sample SHN4). Orange arrows show corrosion/dissolution minerals. Drill core abbreviation: SHN = Sangerhausen.

58.9 wt %) compared to Allstedt (60–66.7 wt %, 64.2 wt %) and Wallendorf (59.2–67.8 wt %, 64.1 wt %) drill core samples. The MgO concentration is slightly higher in the Sangerhausen (1–3.5 wt %, 1.9 wt %) compared to the Allstedt (0.9–1 wt %, 0.9 wt %) and Wallendorf (1.1–1.5 wt %, 1.3 wt %) drill core samples. The CaO concentration in the Sangerhausen (5.4–19 wt %, 12.2 wt %) and Allstedt (10.4–12.9 wt %, 11.8 wt %) drill core samples is nearly twice as high as the Wallendorf drill core samples (4.5–9.4 wt %, 6.5 wt %). The MnO concentration is similar in the Sangerhausen (0.2–0.7 wt %, 0.4 wt %) and Allstedt (0.3–0.4 wt %, 0.4 wt %) drill cores but is lower in the Wallendorf drill core samples (0.1–0.3 wt %, 0.2 wt %). The Fe_2O_3 concentration in the Sangerhausen (0.8–2.1 wt %, 1.4 wt %), Allstedt (1.2–1.6 wt %, 1.4 wt %), and Wallendorf drill core samples (1.6–2.2 wt %, 1.9 wt %) is comparable. The concentration of Al_2O_3 is slightly lower in

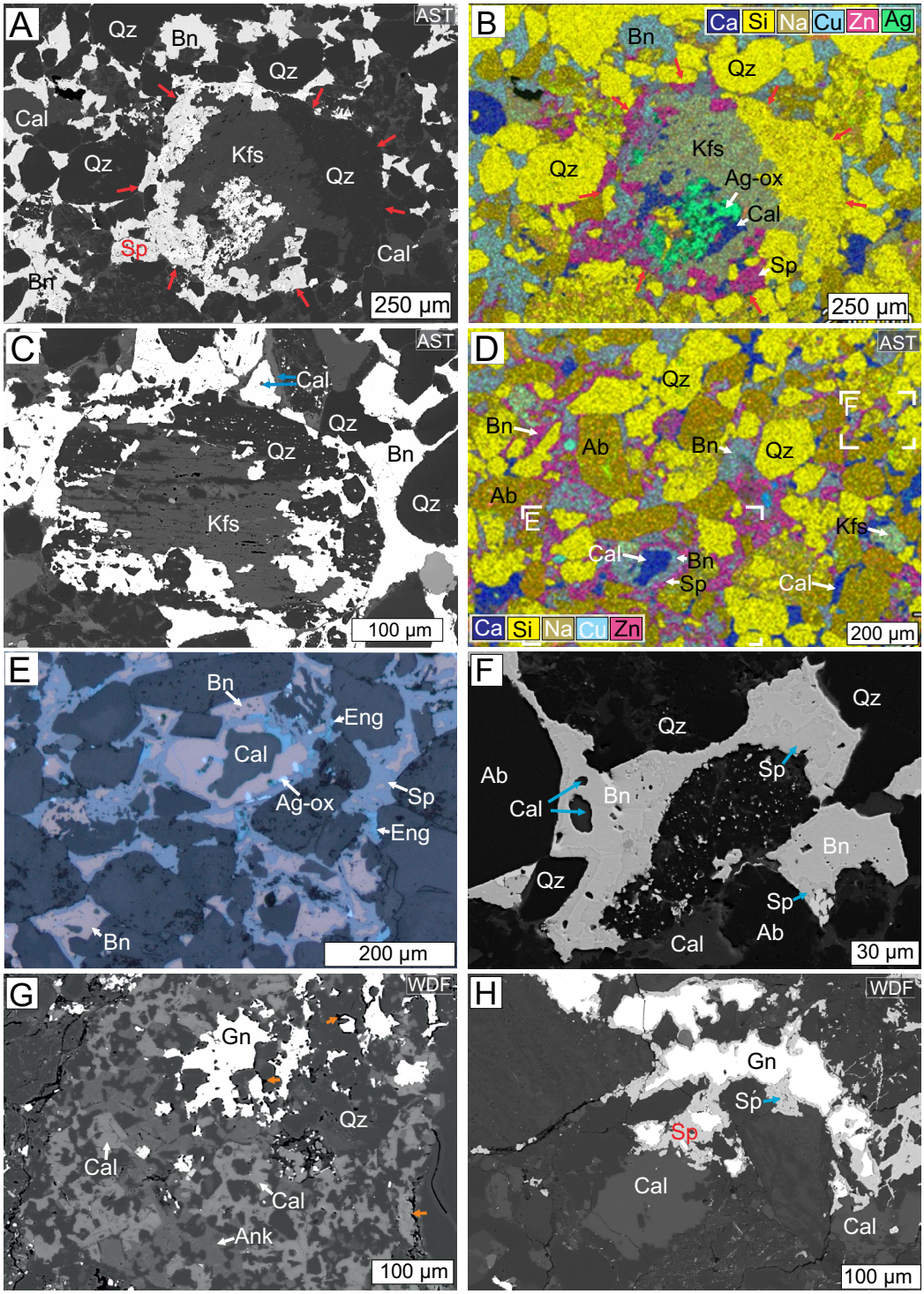

Fig. 6. Sulfide mineralization in the Rotliegend sandstone (S1) from Allstedt (AST) and Wallendorf (WDF) drill core samples. (A) Backscattered electron (BSE) image showing partial replacement of a rounded detrital clast (red arrows) of K-feldspar (Kfs) and calcite (Cal) cement by bornite (Bn) and sphalerite (Sp) (sample AST3). (B) A false-color element map of the same image shown in A, which helps differentiate between the Zn and Cu sulfides and different clast compositions (quartz vs. K-feldspar) (sample AST3). (C) A detrital clast of K-feldspar that has been partially replaced by quartz (Qz) and bornite (sample AST3). (D) A false-color element map showing albite (Ab) and quartz clasts that are cemented by bornite and sphalerite (sample AST3). (E) Reflected-light photomicrograph showing sulfide minerals cementing detrital clasts. Bornite and sphalerite are the main sulfide minerals, with minor enargite (Eng) and very rare silver oxide (Ag-ox). (sample AST3). (F) A BSE image showing minor inclusions of calcite within the sulfide cement of bornite and sphalerite (sample AST3). (G) A BSE image showing ankerite (Ank) and calcite cement preferentially replaced by galena (Gn) in a large detrital quartz clast. The orange arrows show intragranular pores. (H) Replacement of calcite cement by sphalerite and galena (Gn) (sample WDF4). Energy dispersive spectrometry false-color elemental map: Ag = silver oxide, Ca = calcite, Cu = bornite, Na = albite, Si = quartz, Zn = sphalerite.

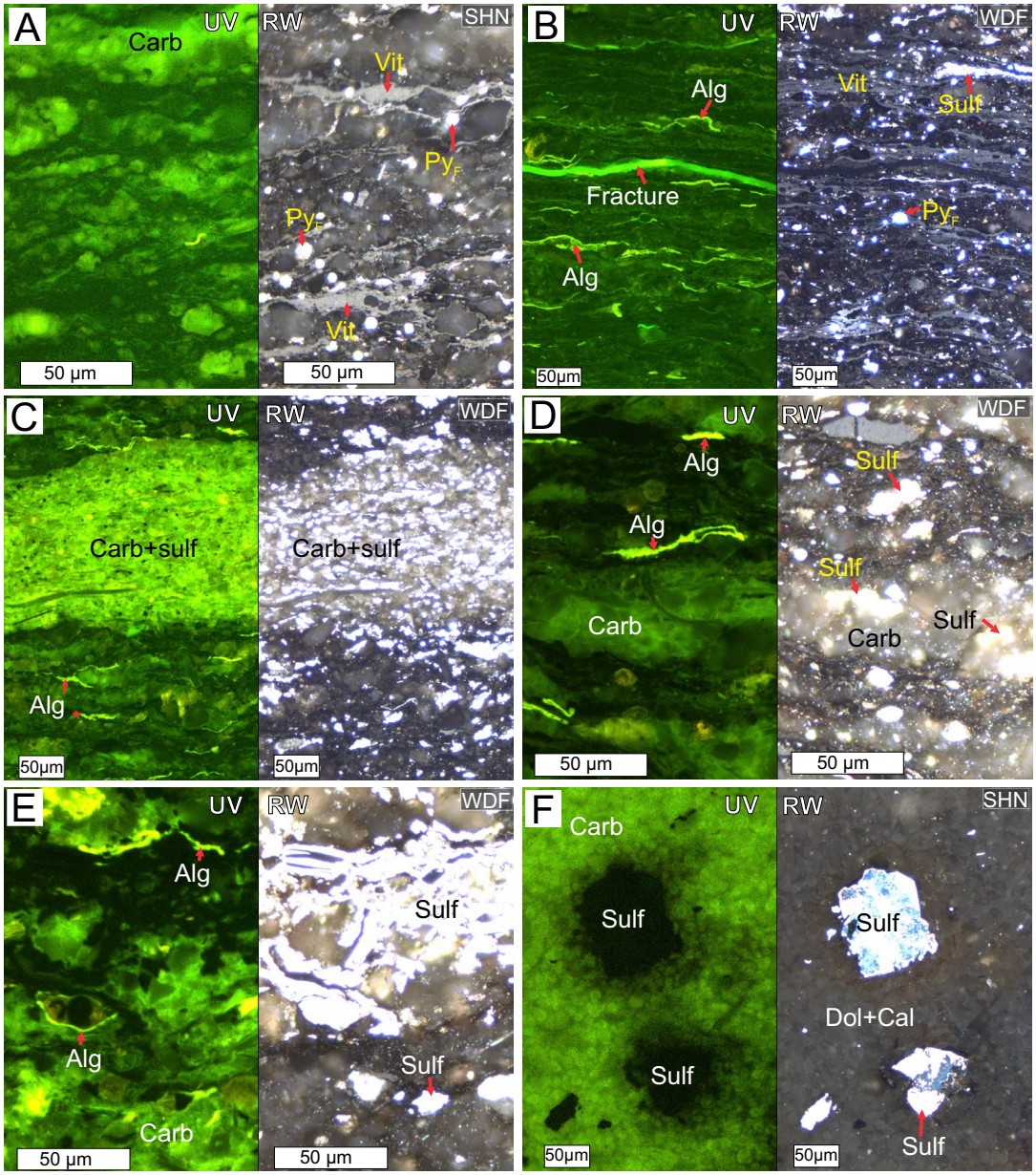

Fig. 7. A series of ultraviolet (UV, left) and reflected white (RW, right) light photomicrographs of the T1 and Ca1 samples from the Sangerhausen (SHN) and Wallendorf (WDF) drill cores. (A) Sample SHN10 in which vitrinite-like macerals (Vit) are parallel to alternating carbonate- and clay-rich laminations. Framboidal pyrite (Py_F) is bright white in RW light. (B) Sample WDF5 showing alginate (Alg) orientated parallel to fine-grained clay-rich laminations. (C) A silt lamination cemented by carbonate (Carb) and sulfides (Sulf) (sample WDF8). (D) Sample WDF10 showing a fine intergrowth of carbonate and sulfide within the fine-grained clay matrix. (E) Sample WDF10 showing sulfides replacing calcite cement. (F) A small vuggy sulfide in the Ca1 limestone from the Sangerhausen drill core (sample SHN16). Cal = calcite, Dol = dolomite.

Fig. 8. Selected backscattered electron (BSE) and false-color element maps of samples in the lower T1. (A) A BSE image of sample SHN9, which shows variation in grain size and organic matter (OM) content between laminations. (B) An element map that can be used to identify the major mineral phases in the image shown in A. (C) Sample AST6, which shows how bornite (Bn) and sphalerite (Sp) have formed preferentially within the coarse-grained lamination. (D) An element map used to interpret the major mineral phases for the image shown in C. (E) Widespread bornite replacement of clasts and carbonate cement within coarse-grained laminations in sample AST6. The insoluble margins of clasts are highlighted by red arrows. (F) Remnant inclusions of calcite (Cal) contained within a clast that has been replaced by bornite. (G) A sulfide-rich lamination of sphalerite and bornite in sample AST6. (H) A BSE image of the contact between sphalerite and bornite in sample AST6. Energy dispersive spectrometry false-color elemental composite maps: Al = kaolinite, Ca = calcite, Cu = bornite, Mg = dolomite, Na = albite, Si = quartz, Zn = sphalerite. Drill core abbreviations: AST = Allstedt, SHN = Sangerhausen. Other mineral abbreviations: Ab = albite, Ap = apatite, Dol = dolomite, Ilt = illite, Kln = kaolinite, Qz = quartz, Pb-ox = lead oxide, Py = pyrite, Py_F = framboidal pyrite.

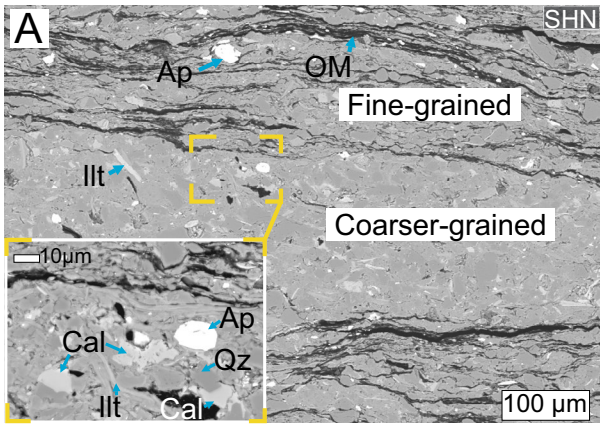

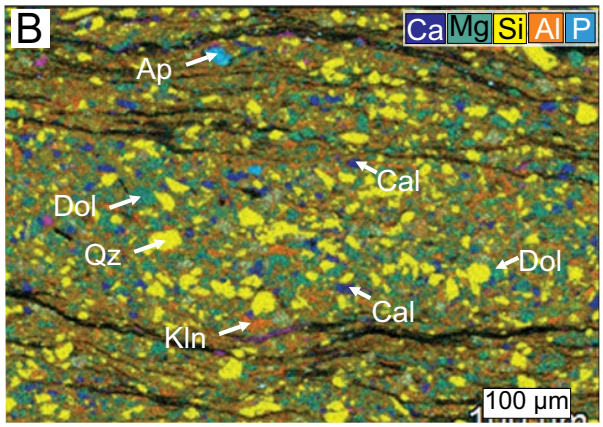

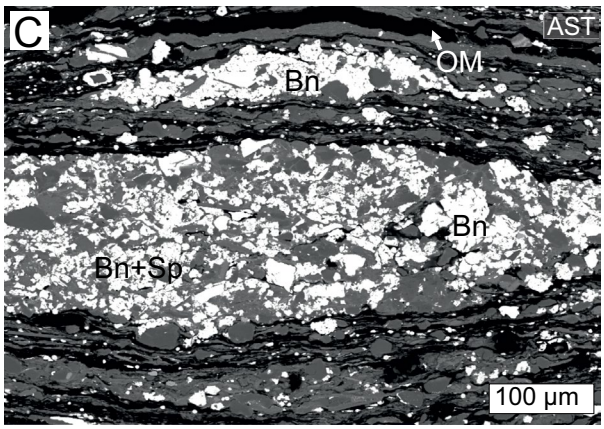

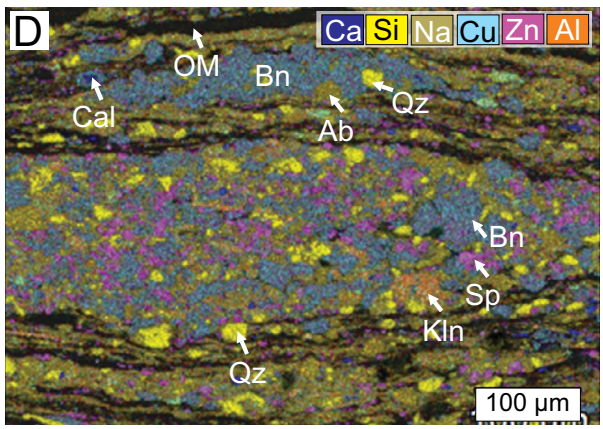

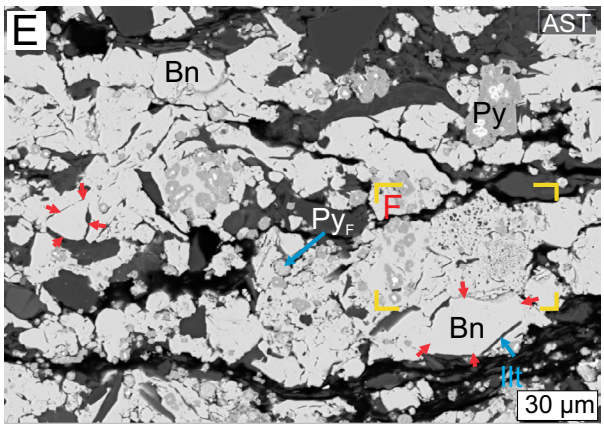

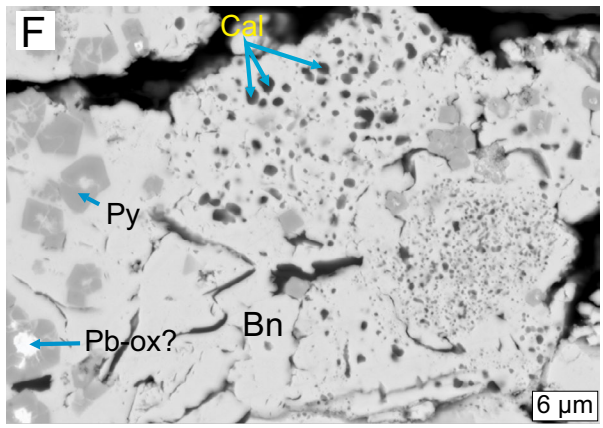

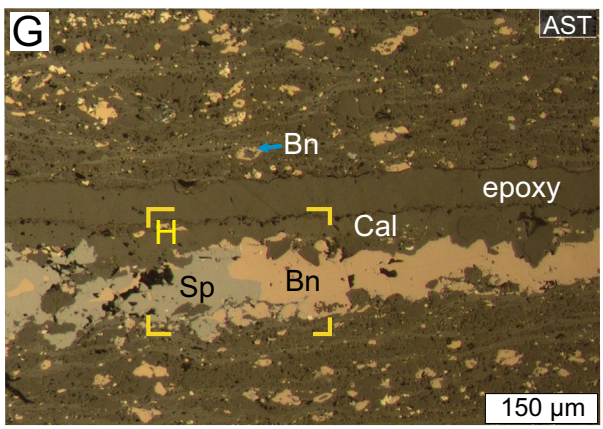

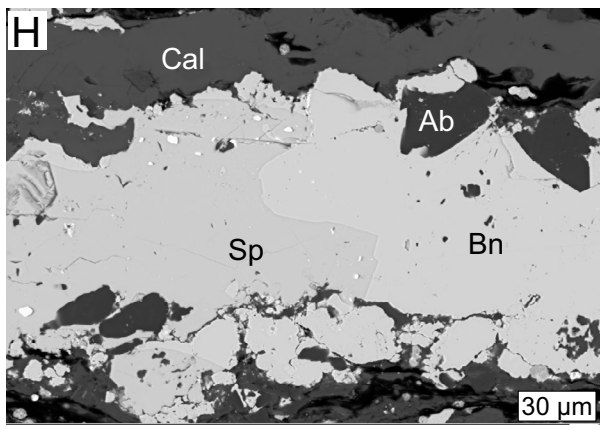

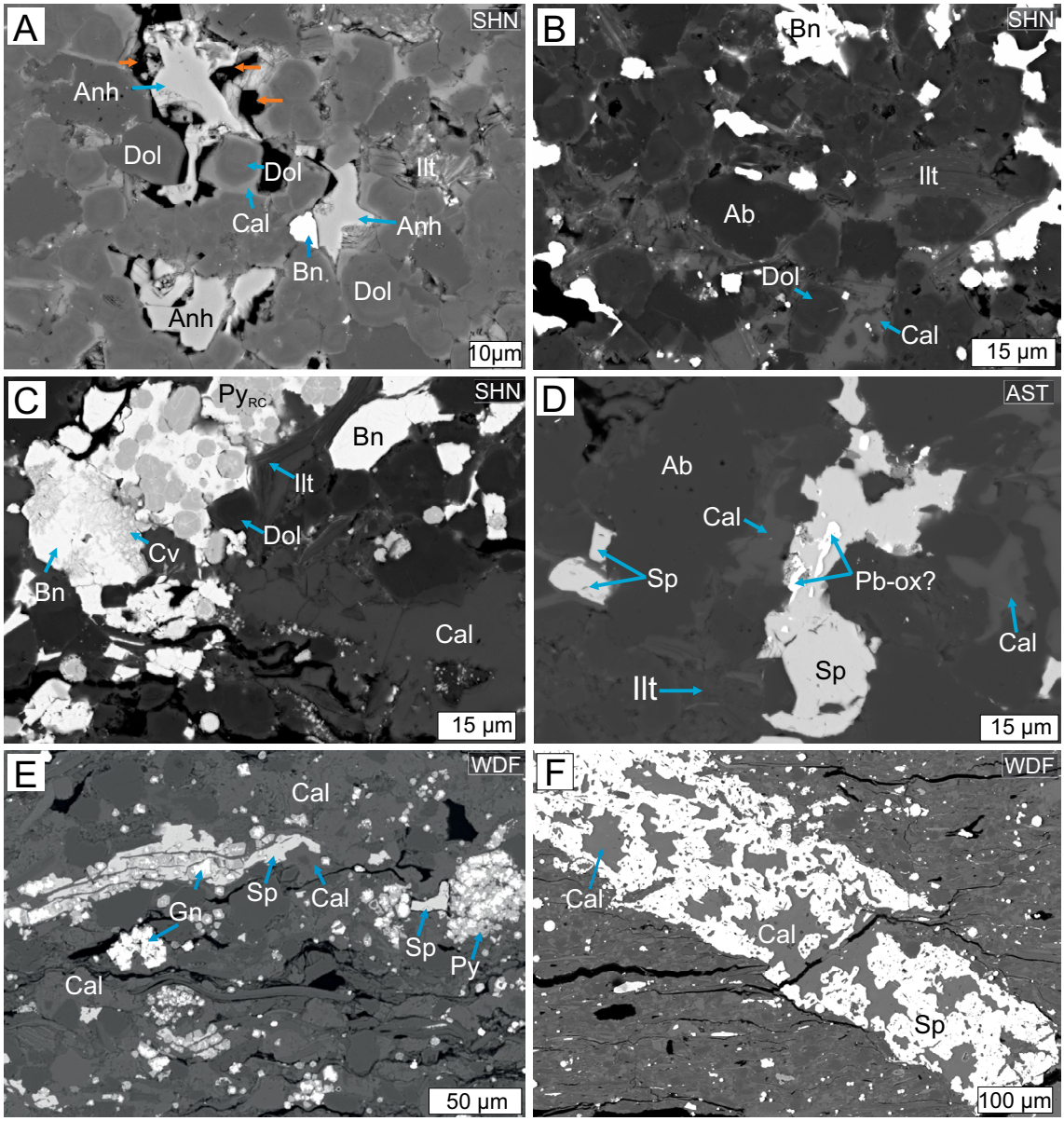

Fig. 9. Selected backscattered electron (BSE) images of samples from the middle and upper T1. (A) Rhombic dolomite (Dol) with calcite (Cal) overgrowth and pore-filling anhydrite (Anh) and bornite (Bn) (sample SHN11). The orange arrows show secondary porosity as a result of anhydrite and calcite dissolution. (B) Detrital albite (Ab) and dolomite cemented by calcite and bornite in the Sangerhausen samples (sample SHN11). (C) Complex assemblage of bornite and covellite (Cv) that has cemented recrystallized diagenetic pyrite (Py_{RC}) (sample SHN11). (D) Pore-filling sphalerite (Sp) that has replaced calcite cement (sample AST9). (E) Sphalerite that has overgrown aggregates of diagenetic pyrite (Py) in sample WDF7. (F) A sulfide veinlet containing sphalerite and calcite in sample WDF9. Drill core abbreviations: AST = Allstedt, SHN = Sangerhausen, WDF = Wallendorf. Mineral abbreviations: Ilt = illite, Gn = galena, Pb-ox = lead oxide.

the Sangerhausen and Wallendorf than in the Allstedt drill core samples (Fig. 13A, B). The minor oxides (TiO_2, mean ~0.4 wt %; P_2O_5, mean 0.1 wt %) have similar concentrations in all drill cores. The Al_2O_3 content is strongly correlated in all drill cores with TiO_2 or K_2O but not with Na_2O (Fig. 13A, C, D). However, the Al_2O_3 content is negatively correlated with CaO/TiO_2 (r^2= –0.85; Fig. 13B). The concentration of base metals (Cu, Zn, and Pb) in the sandstone samples is generally very low, except for those samples adjacent to the T1 (Cu = 1% in SHN7, Cu = 0.9 wt % in AST3, and Cu = 0.7 wt % and Pb = 0.6 wt % in WDF4; Fig. 11A-C).

Trends in major elements and base metal composition in the Kupferschiefer (T1): The T1 samples preserve a very strong correlation between Al_2O_3 and TiO_2 (r^2 = 0.99; Fig. 13A). The lower T1 has a low CaO content in all drill cores. The highest CaO (19.1 wt % in WDF7) and MgO (7.5 wt % in SHN11) concentrations are in the middle T1 samples, but upper T1 samples from Allstedt (8 wt % in AST13) have similarly high values. All samples have a strong negative correlation between the CaO/TiO_2 ratio and Al_2O_3 (r^2 = –0.85; Fig. 13B).

Lower base metal concentrations are observed in the lowermost T1 samples in all drill cores, except samples

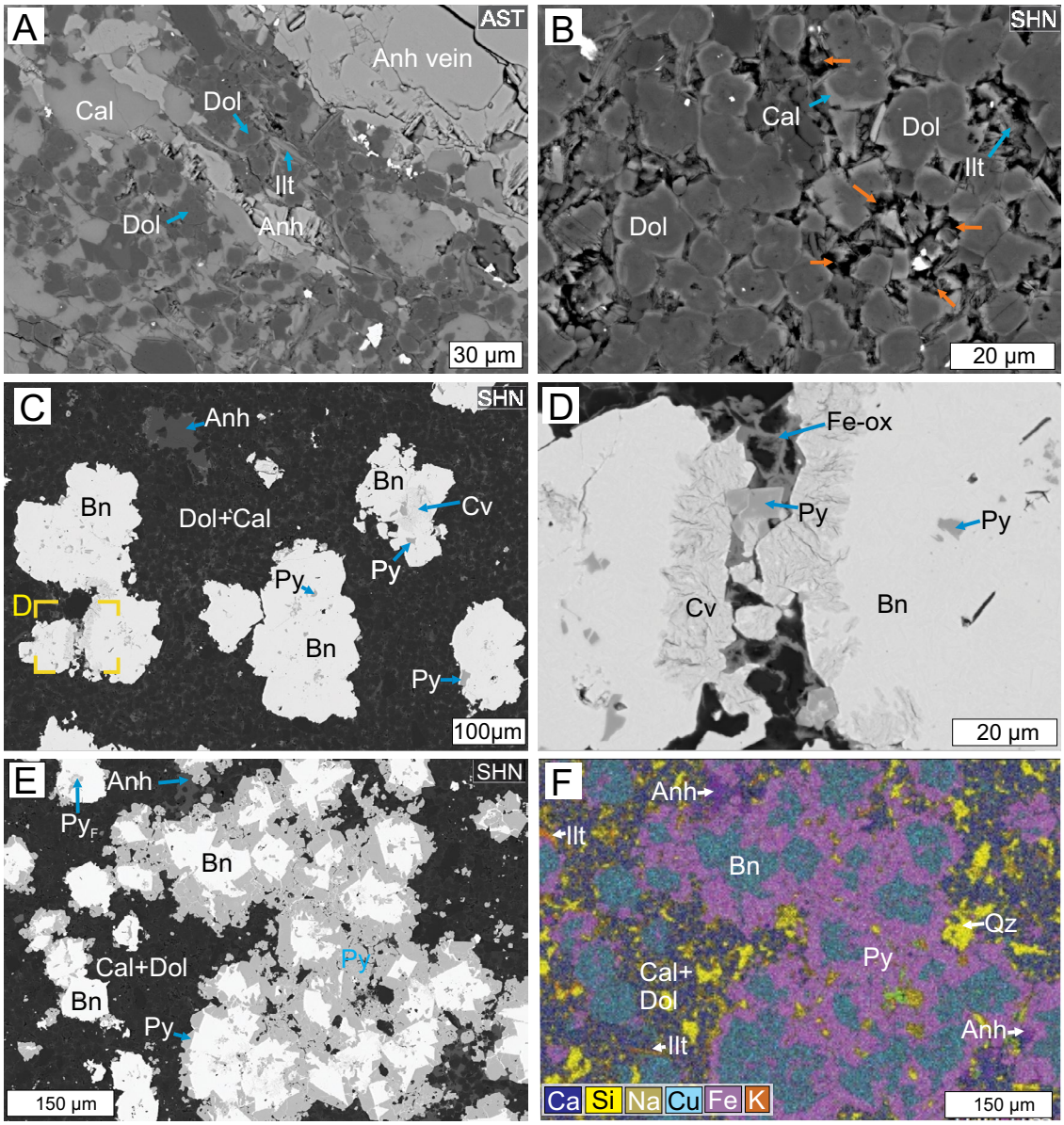

Fig. 10. Selected backscattered electron (BSE) images and a false-color element map for samples from the Zechstein limestone (Ca1). (A) Dolomite (Dol) that has been cemented by calcite (Cal) and crosscut by an anhydrite (Anh) vein (sample AST15). (B) Interlocking rhombic dolomite crystals with calcite rims, with minor pore-filling authigenic illite (Ilt) highlighted by the blue arrow (sample SHN16). Orange arrows highlight dissolution of calcite and dolomite cements. (C) Large vuggy sulfide infill comprising bornite (Bn), covellite (Cv), and pyrite (Py) within the host rock of dolomite and calcite (Dol + Cal) (sample SHN16). (D) Bornite crystals that have been altered to covellite, with minor Fe oxide (Fe-ox) forming overgrowths to dolomite (sample SHN16). (E) Coarse-grained aggregates of bornite and pyrite within calcite and dolomite host rock (sample SHN16). (F) A false-color element map used to interpret the major mineral phases shown in E. Energy dispersive spectrometry false-color elemental composite maps: Ca = calcite, Cu = bornite, Fe = pyrite, Na = albite, S = anhydrite, Si = quartz. Drill core abbreviations: AST = Allstedt, SHN = Sangerhausen. Other mineral abbreviations: Py_F = framboidal pyrite.

with abundant layered sphalerite with pyrite in coarser-grained laminations such as in WDF5 (Zn = 3.1 wt %; Figs. 11, 13E). The entire T1 in the Sangerhausen drill core in the Cu zone has elevated Cu concentrations (max. 1.2 wt % in SHN11; Fig. 11A). The Allstedt samples are Cu rich in the lower T1 (max. 2.4 wt % in AST6), Zn rich in the middle T1 (max. 2.4 wt % in AST9), and Pb rich in the upper T1 (max. 0.7 wt % in AST13), reflecting the vertical sulfide zoning (Fig. 11B). The Wallendorf samples have higher Zn (max. 2.5 wt %) and Pb (max. 0.9 wt %) concentrations, both increasing toward the upper T1, in sample WDF10 (Fig. 11C). However, sample WDF5 in the lower T1 has exceptionally high Zn concentration (3.1 wt %) because of layered sphalerite (Fig. 11C).

The total sulfur, total organic carbon, and total inorganic carbon contents are presented in the supplementary data file (Mohammedyasin et al., 2022). The highest total sulfur and total inorganic carbon content, consistent with the abundant

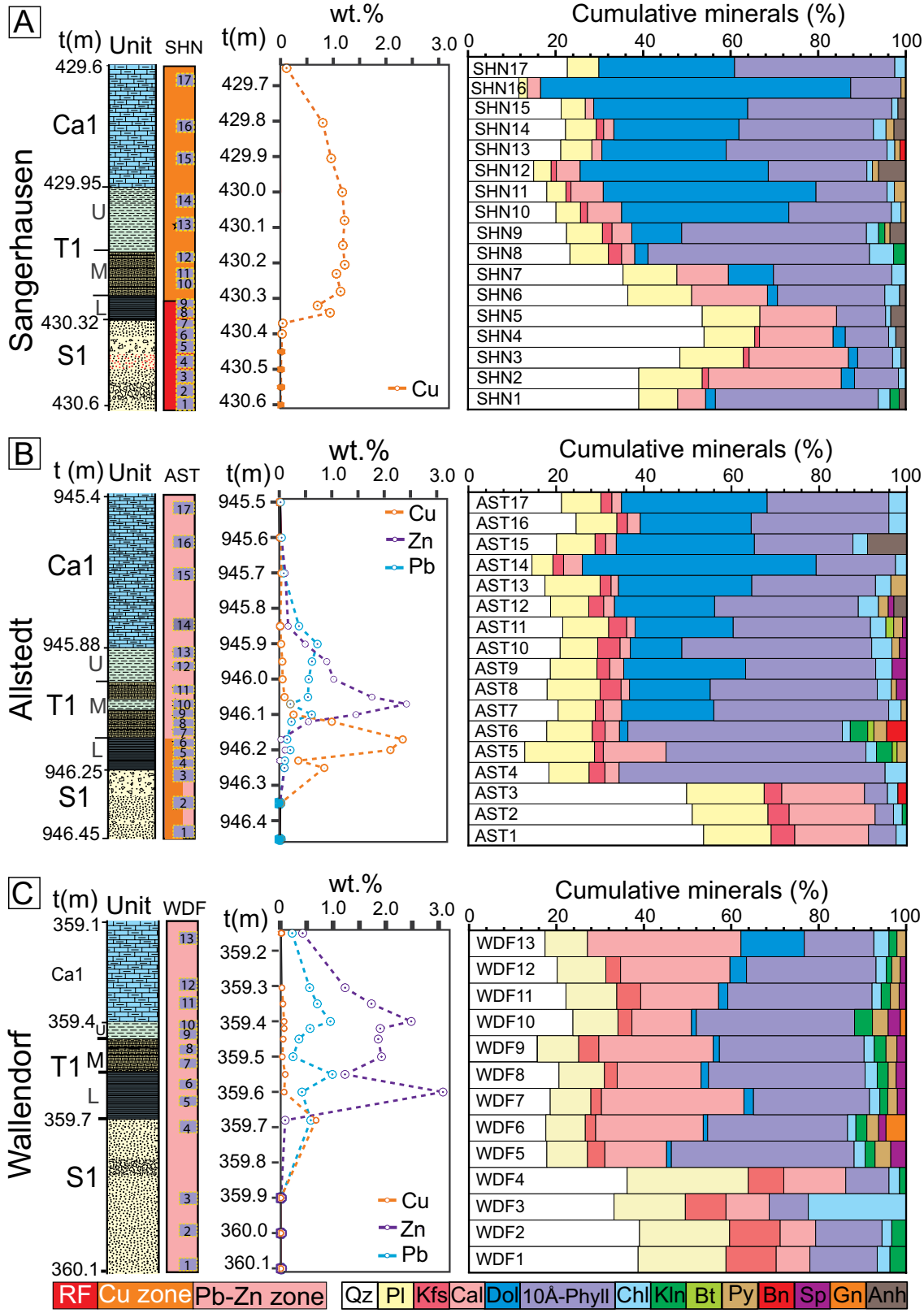

Fig. 11. Graphical logs for Sangerhausen (SHN; A), Allstedt (AST; B), and Wallendorf (WDF; C) drill core samples showing base metal concentrations (wt %) and modal mineralogy (%) from quantitative X-ray diffraction. 10Å-Phyll = 10Å-phyllosilicate (muscovite + phlogopite + illite). Anh = anhydrite, Bn = bornite, Bt = biotite, Cal = calcite, Chl = chlorite, Dol = dolomite, Gn = galena, Kfs = K-feldspar, Kln = kaolinite, Pl = plagioclase, Py = pyrite, Qz = quartz, Sp = sphalerite, RF = Rote Fäule, t = depth (m).

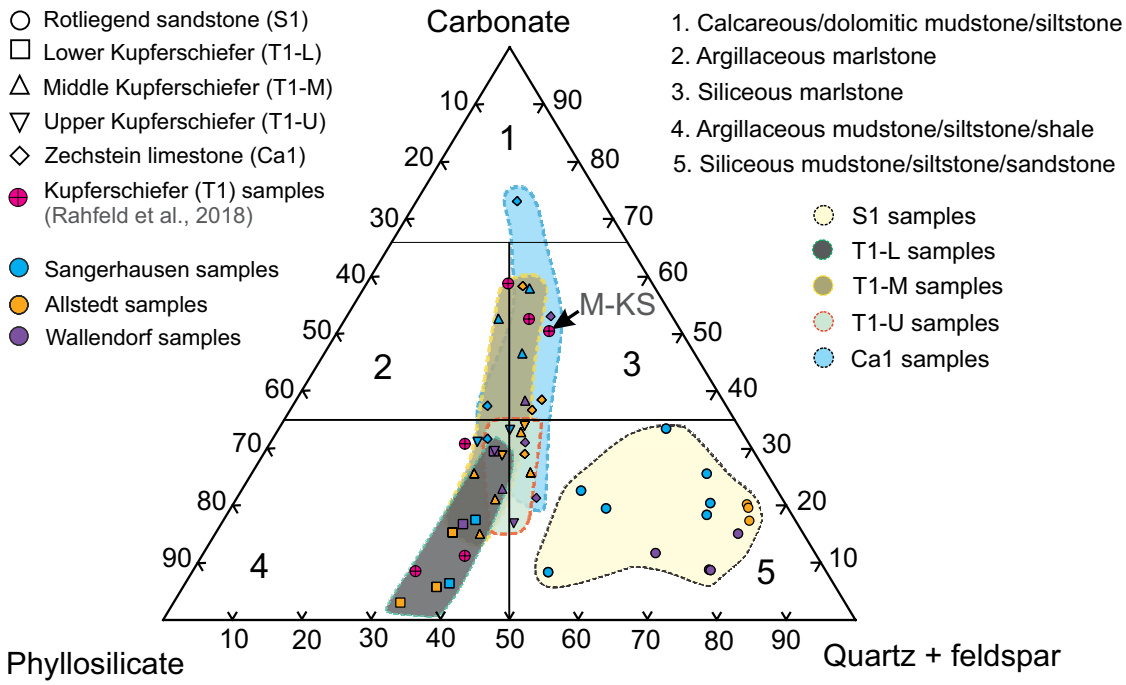

Fig. 12. A ternary diagram for major mineralogical composition (carbonate, phyllosilicate + quartz, feldspar) for samples from all three drill cores. Each unit/subunit is assigned by a specific shape and shaded with the same background color, where the color of each shape represents the drill core. Phyllosilicate = 10Å-phyllosilicate (muscovite, phlogopite, illite) + chlorite. The T1 samples from Mansfeld (M-KS), Wettelrode, Polkowice, Rudna, and Lubin Kupferschiefer districts from Rahfeld et al. (2018) are plotted together for comparison.

carbonate, is mostly observed in samples from the middle T1 in all drill cores (Fig. 13E, F). The total organic carbon content increases toward the lower T1 in all drill cores where fine-grained laminations are organic matter rich. The Allstedt drill core samples contain higher total organic carbon content (max. 20.3 wt % in AST5) compared to the Wallendorf (12.6 wt % in WDF6) and Sangerhausen (7.2 wt % in SHN9) drill core samples.

Trace element composition: The concentration of trace elements in the S1 is relatively lower and uniform compared to the T1 samples in all drill cores. Only U and Mo in samples from the Allstedt and Ga and Nb in samples from the Wallendorf have higher concentrations.

The concentration of trace elements varies in the different subunits of the T1. This has been further evaluated using the relative change in trace elements (TE_{Δ}) from the global median black shale (MBS) of all host rock types (Ketris and Yudovich, 2009) calculated by normalizing to Ti [$TE_{\Delta} = ((TE/Ti)_{sample} - (TE/Ti)_{MBS})/(TE/Ti)_{MBS}) \times 100$]. The MBS is preferred here because other shale normalizations have very different trace element concentrations that may cause different paleoredox interpretations (Slack et al., 2021). Titanium is used here for normalizing because it has a nearly perfect correlation ($r^2 = 0.99$) with Al in the T1 samples, and Al was not reported in the MBS database of Ketris and Yudovich (2009).

Most of the trace elements (e.g., Mo, U, V, Ni, As, and Tl) have very large to extreme positive changes in the lower T1, except Mo and Tl in the Sangerhausen drill core (see Table 1). Cobalt and Cd, however, have very large to extreme positive changes in specific sulfide zones. For example, Co in the Cu zone from the Sangerhausen drill core and Cd in the Zn-Pb zone from the Allstedt and Wallendorf drill cores show extreme enrichments (Table 1; Fig. 14A-C). The highest TE_{Δ} values correspond to the highest base metal concentrations. These enrichments are found mostly in the middle T1, which corresponds with the high-grade sulfide mineralization. In contrast, the Cu zone shows depletion in Cd, i.e., the entire T1 in the Sangerhausen and lower T1 in the Allstedt drill core samples (Fig. 14A). Further investigation on the trace element composition of base metal sulfides is required to accurately constrain a genetic relationship associated with the hydrothermal input.

The relationship between several redox-sensitive trace elements (RSTEs; Mo, U, V, Cr, Ni, and As) and base metals has been tested (cf. Stüeken et al., 2020), and apart from Mo and Cu (Fig. 14D-G) there is no correlation. Rather, the concentration of several RSTEs covaries with total organic carbon content and increases toward the lower T1 (e.g., Fig. 15A-C). The lower T1 samples from the Sangerhausen drill core are depleted only in Mo, but not U (Fig. 15A). The enrichment factor (EF) of selected RSTEs (trace elements = U, Mo, Ni, V, Cr) was calculated relative to Post Archean Australian Shale (PAAS; Taylor and McLennan, 1985) on Al-normalized basis [$TE_{EF} = (TE/Al)_{sample}/(TE/Al)_{PAAS}$]. Enrichment factors of Mo, U, V, Cr, and Ni generally increase toward the lower T1 (Table 1; Fig. 15). However, Mo_{EF} and Ni_{EF} values are exceptionally low in the lower T1 in the Sangerhausen drill core samples (Table 1). The U_{EF} and Mo_{EF} values in the middle and upper T1 are similar in the Wallendorf drill core samples (Table 1). Most of the Ca1 samples, however, show Mo depletion relative to T1 samples (Fig. 15A-C).

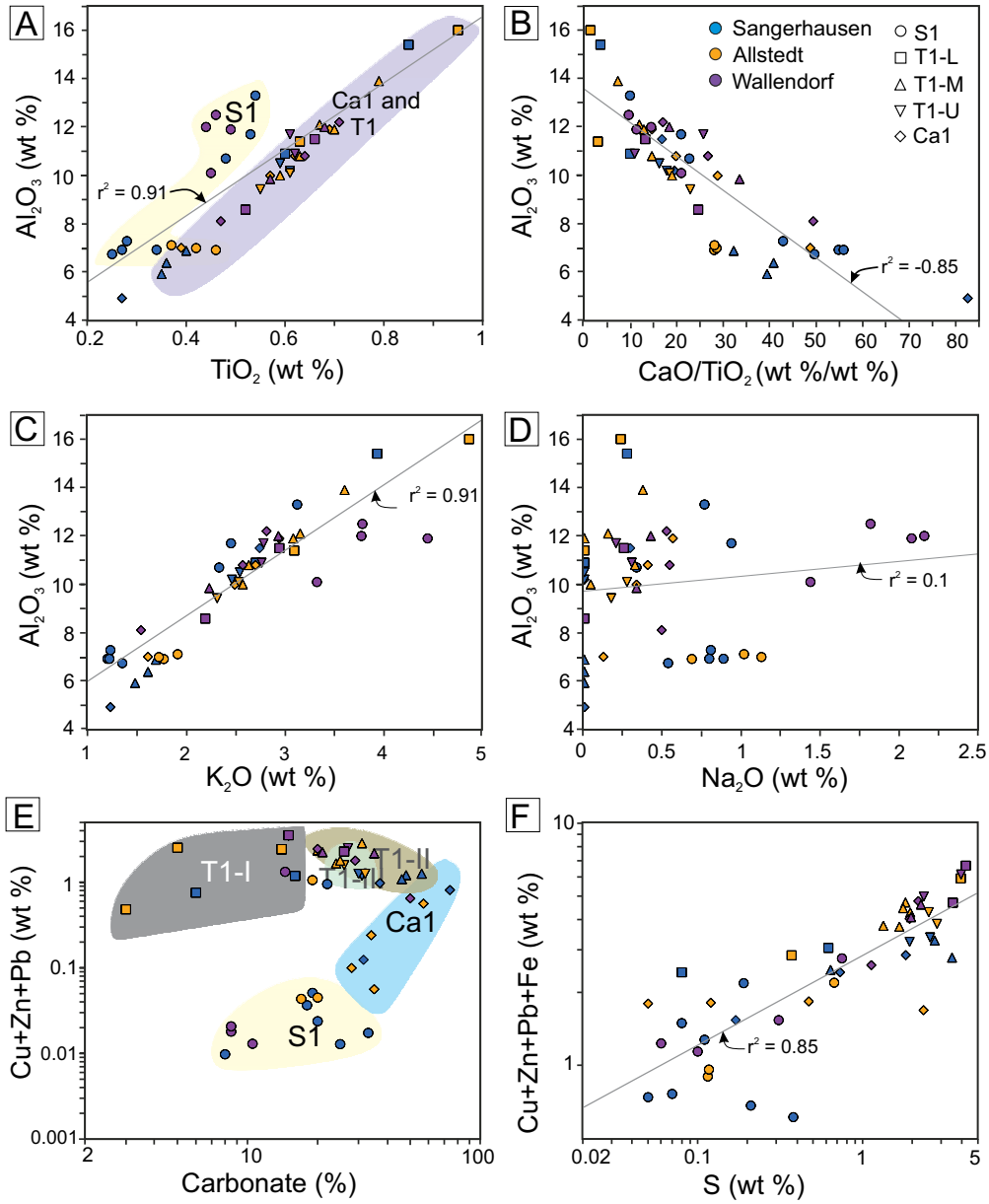

Fig. 13. A series of bivariate plots for major element composition. (A) TiO_2 (wt %) vs. Al_2O_3 (wt %). The pale yellow and purple denote composition fields for S1 and Ca1 + T1, respectively. (B) CaO/TiO_2 (wt %/wt %) vs. Al_2O_3 (wt %). (C) K_2O (wt %) vs. Al_2O_3 (wt %). (D) Na_2O (wt %) vs. Al_2O_3 (wt %). (E) Carbonate (quantitative X-ray diffraction, %) vs. Cu + Zn + Pb (wt %). (F) S (wt %) vs. Cu + Zn + Pb + Fe (wt %). Fe excluded in this figure to acount only carbonate replacement by the Cu and Zn-Pb sulfides. T1-L = lower Kupferschiefer, T1-M = middle Kupferschiefer, T1-U = upper Kupferschiefer.

Discussion

The petrographic observations together with the mineralogical and geochemical trends have been used to unravel the relative timing and formation processes of diagenetic and hydrothermal mineral assemblages in the S1, T1, and Ca1 units (Fig. 3). These data sets will be combined to investigate the major diagenetic events and style of sulfide replacements in the main ore-bearing units from the Saale subbasin, Eastern Germany.

Diagenetic evolution of the Rotliegend sandstone (S1)

The primary composition of sandstone is controlled by the regional geologic setting, hydrology, and climate of the source area (Dickinson, 1970; Dickinson and Suczek, 1979; Dickinson et al., 1983). Similar to sandstones deposited in other semiarid to arid environments (Morad et al., 2010), the Rotliegend sandstones are mineralogically immature and characterized by high content of feldspar and rock fragments (Fig. 4A-D). The high proportion of silicate clasts means the Rotliegend sandstones were likely mechanically stable but chemically unstable (Worden and Morad, 2003), consistent with the lack of compacted grains (e.g., Fig. 4A-D).

Calcite (± dolomite) is the most abundant intergranular pore-filling carbonate cement between detrital clasts. The calcite cement likely formed shortly after deposition during

Table 1. Trace Element Change (TE_{Δ}, %) and Trace Element Enrichment Factor (EF) Calculated Relative to the Median Black Shale (Ketris and Yudovich, 2009) and Post-Archean Australian Shale (Taylor and McLennan, 1985), Respectively

	Sangerhausen			Allstedt			Wallendorf		
TE_{Δ}	T1-L	T1-M	T1-U	T1-L	T1-M	T1-U	T1-L	T1-M	T1-U
Li	67.0	48.0	22.4	103.8	87.0	95.4	84.9	88.9	108.8
Cd	–94.4	–80.3	–83.2	–65.8	711.6	453.8	1,677.8	1,464.8	1,751.3
Ba	–53.6	10.1	173.6	–60.1	–45.3	–22.5	–66.0	–64.0	–63.3
Tl	82.9	539.4	135.6	390.5	137.7	195.5	332.5	12.6	89.6
Bi	–8.1	746.7	–79.5	110.6	–69.7	–65.0	–67.5	–71.4	–55.9
Th	13.4	27.1	19.1	7.9	14.9	26.3	20.0	12.8	36.5
U	651.1	423.3	27.6	1,419.8	170.4	–12.7	370.1	141.5	102.1
Be	105.3	66.8	46.0	121.4	14.8	8.3	117.9	71.5	99.0
Sc	–13.7	–12.0	–27.0	–32.5	–40.0	–42.1	–31.9	–36.8	–30.8
Cr	69.3	26.0	–28.3	18.3	–20.4	–45.0	19.6	–12.7	–9.2
Co	670.1	1,729.0	551.9	876.3	179.7	106.9	1,362.3	313.1	147.2
Ni	82.4	207.8	37.0	186.7	108.9	–0.9	205.2	70.0	67.0
Ga	–7.3	–13.1	–24.4	–26.2	–32.9	–36.5	–19.3	–27.2	–18.2
Rb	80.9	80.3	56.7	29.2	26.6	18.9	29.9	21.9	46.9
Sr	–29.3	112.9	50.6	–64.3	–34.9	–5.6	–35.8	–24.2	–41.8
Nb	41.2	26.4	13.7	7.5	0.2	–5.4	13.4	–0.9	15.3
Mo	72.6	692.3	177.3	1,094.7	611.4	37.2	431.2	68.1	81.3
Sn	–23.9	–21.6	–27.3	–33.4	–31.8	–32.3	–30.9	–32.2	–20.5
Sb	–66.2	–16.6	145.2	124.0	–40.4	–28.7	245.2	46.5	121.8
Cs	223.1	225.3	175.0	298.4	247.4	217.4	294.8	258.8	373.2
V	471.4	381.4	1.1	431.8	95.9	–29.0	349.6	102.4	66.0
As	131.2	303.1	123.8	427.6	–27.6	39.7	1,459.7	260.3	244.5
TE_{EF}									
Mo_{EF}	71.8	266.8	121.4	600.8	297.6	60.6	247.1	72.1	73.9
U_{EF}	44.1	31.7	7.7	71.6	41.5	5.4	28.5	14.3	11.2
Ni_{EF}	5.2	9.0	3.8	6.1	5.9	2.8	8.7	4.6	4.4
V_{EF}	16.5	13.7	3.0	13.2	6.0	2.2	13.9	5.9	4.7
Cr_{EF}	3.1	2.3	1.4	2.5	1.5	1.1	2.3	1.6	1.6

the early stages of diagenesis, as it has occluded precompaction intergranular porosity (Worden et al., 2020). The random shape and orientation of clasts further indicates minimal compaction took place before calcite cementation (Fig. 4A-D). This is most clearly highlighted by the preservation of undeformed muscovite grains (e.g., Fig. 5B). The absence of clay rims means that porosity was occluded by the calcite cement before clasts could be altered by undersaturated pore fluids (e.g., Waldmann and Gaupp, 2016).

Following a marine transgression, early diagenetic carbonate cements can often develop in aeolian and fluvial sandstones (Ketzer et al., 2002, 2003b). The diffusion of Ca^{2+} and HCO_3^- from overlying seawater is commonly enhanced by slow sedimentation rates associated with a sea-level highstand (e.g., Ketzer et al., 2002; El-Ghali et al., 2006, 2013). The patchy anhydrite cement that formed together with the calcite and barite cement may suggest the involvement of a partially evaporated seawater-derived fluid (Fig. 4E, F). Similarly, the strong enrichment of deuterium in *n*-alkanes (δD values up to –36‰) and isoprenoids (δD values up to –20‰) in T1 samples proximal to the Rote Fäule from the Spremberg area (Eastern Germany) has been used to show interaction between organic matter and evaporitic seawater at temperatures less than 110°C (Poetz et al., 2022). The evaporated seawater could derive from short-lived marine ingressions at the end of Rotliegend deposition (e.g., Stollhofen et al., 2008) or during the more widespread deposition of the overlying Zechstein salt (e.g., Sullivan et al., 1994).

There is a minor component of euhedral dolomite, which is commonly overgrown by calcite (e.g., Fig. 4E, F, H). The dolomite could have formed via a number of pathways—for example, mixing between meteoric, evaporative, and marine waters (Morad et al., 2000)—but it is also possible that it formed via Mg sources from the alteration of mafic rock fragments (e.g., Fig. 4C). The higher dolomite contents in the Sangerhausen and Allstedt samples relative to the Wallendorf samples may indicate differences in the Mg/Ca ratio of seawater between marginal marine and basinal settings, respectively. The precipitation of calcite rather than dolomite can be favored during significant seawater diffusion, which may be controlled by the primary porosity and permeability. The growth of trace hematite on euhedral dolomite shows that hematite formation postdates the euhedral dolomite (probably an initial phase; Fig. 5C). Therefore, the paragenetic relationship between dolomite and hematite suggests that the hematite did not form as the earliest phase i.e., as a detrital grain coating. The intergrowth of most of the hematite within later-formed zones of the calcite cement indicates that hematite mostly postdates the first extensive calcite cement but could overlap or predate the last phase of calcite cementation (Figs. 3, 4E-H, 5B, C). The origin of hematite in the Rote Fäule could be linked to ferrous Fe oxidation that generates acidity (H^+) that would be buffered by the dissolution of carbonate in the host rocks. The ferrous Fe could be released during the dominant Cu sulfide mineralogy transitions from chalcopyrite to bornite and then to chalcocite (Zhang et al., 2021). Alternatively, the dissolution or breakdown of mafic rock fragments would have released Fe that could have been incorporated into hematite.

The other diagenetic feature in the Rotliegend unit is the alteration of feldspar grains. The alteration of detrital plagio-

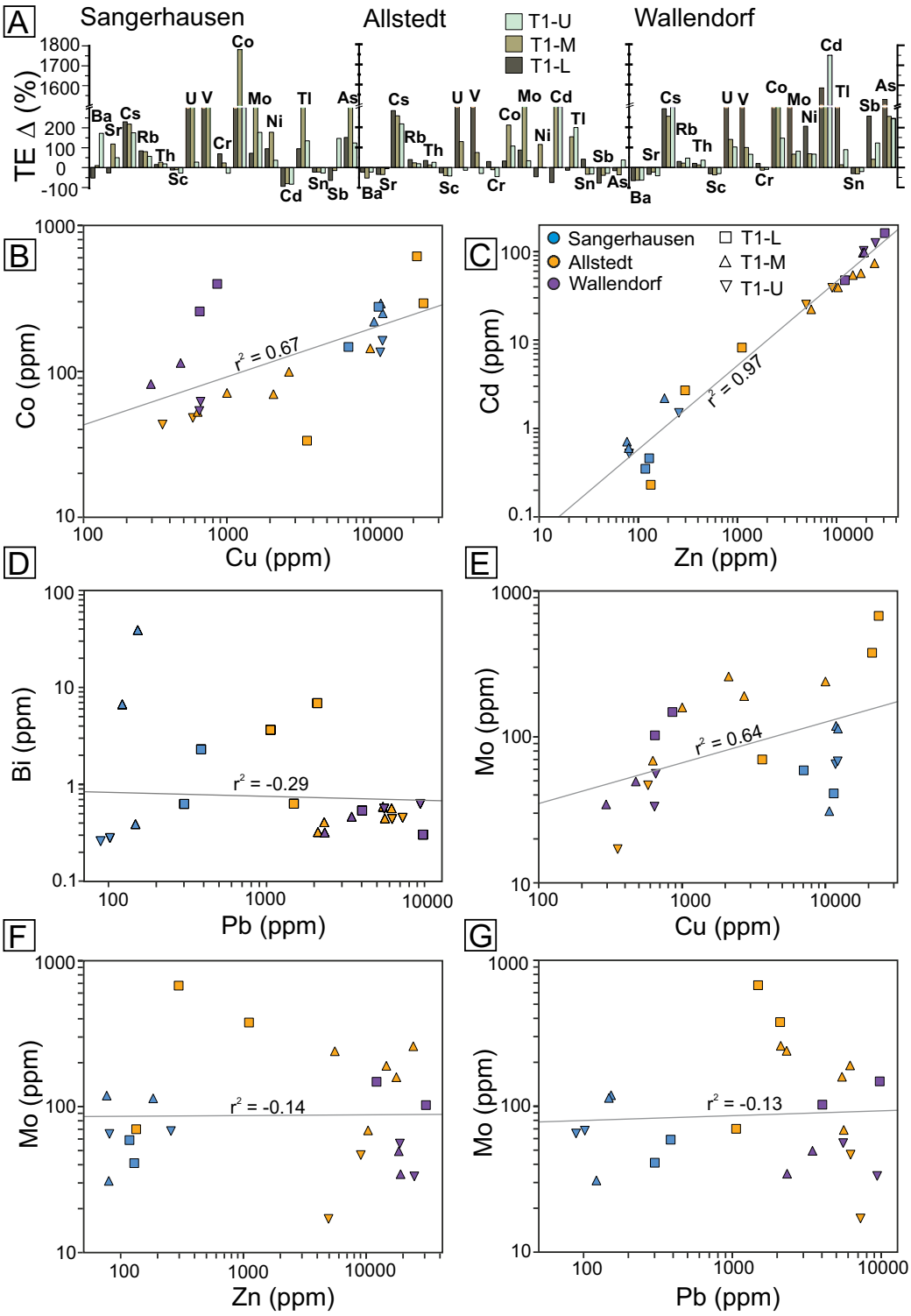

Fig. 14. (A) Comparison of trace element change (TE_{Δ}, %; refer to text for details) calculated relative to the median black shale (Ketris and Yudovich, 2009) in the subunits of the T1. (B) A bivariate plot of Cu (ppm) vs. Co (ppm). (C) A bivariate plot of Zn (ppm) vs. Cd (ppm). (D) A bivariate plot of Pb (ppm) vs. Bi (ppm). (E) A bivariate plot of Cu (ppm) vs. Mo (ppm). (F) A bivariate plot of Zn (ppm) vs. Mo (ppm). (G) A bivariate plot of Pb (ppm) vs. Mo (ppm).

clase follows cleavage planes and twinning surfaces (Fig. 4A), consistent with faster dissolution along weak surfaces due to excess surface energy (Morad et al., 1990). Detrital albite is also sometimes replaced by calcite with minor anhydrite and barite, mostly intergrown with kaolinite (Fig. 5E, F). These alteration assemblages may have originated from feldspar-undersaturated fluids, such as residual meteoric water that was trapped in pores before calcite cementation, or from organic

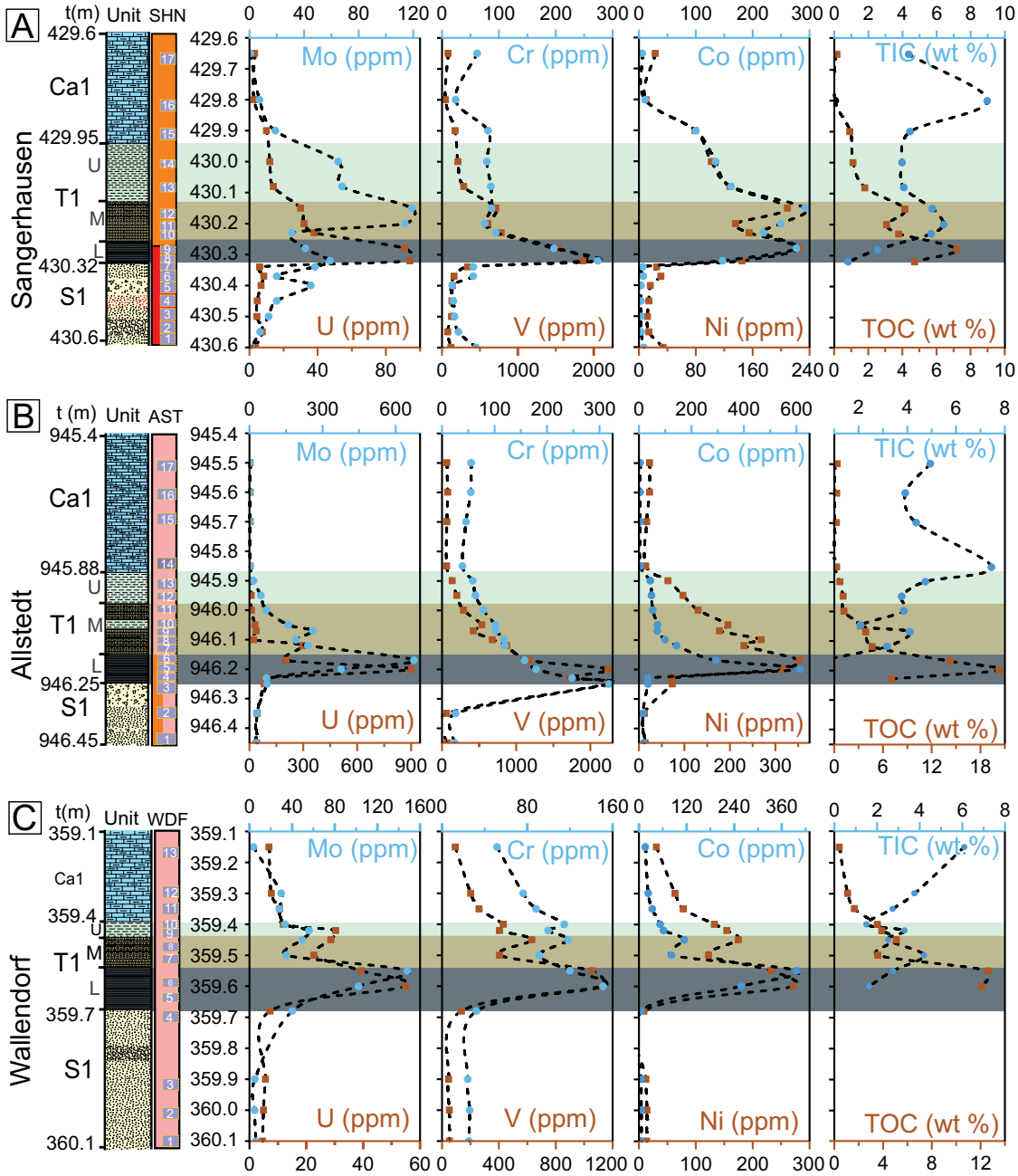

Fig. 15. Downhole plots of selected trace elements (Mo, U, Cr, V, Co, and Ni), total organic carbon (TOC) and total inorganic carbon (TIC) for Sangerhausen (SHN; A), Allstedt (AST; B), and Wallendorf (WDF; C) drill cores. Notice the different scales for different drill holes.

acids that infiltrated from the overlying Kupferschiefer unit. However, several lines of evidence suggest that feldspar alteration mainly postdates carbonate cementation.

1. Dissolution of calcite cement and formation of a serrated dissolution contact with the altered volcanic rock fragment could be explained by local in situ acid generation either released from the overlying organic matter in the T1 or during clay precipitation (green arrow, Fig. 4B).
2. Precompaction dissolution of clasts would lead to greater susceptibility to deformation of clasts during burial, which is not observed, as clasts retain their original shape (Fig. 4A, B, D).
3. Clast dissolution and replacement was restricted to specific clasts under closed-system conditions, i.e., mafic volcanic rock fragments are more susceptible to dissolution and replacement (e.g., Fig. 4B, C).

The precipitation of illite can be explained by $[a(K^+)/a(H^+)]$ ratio in the solution during fluid-rock interactions (Lanson et al., 2002). Textural evidence suggested that early illite and chlorite formed early in the diagenetic sequence as a result

of alteration or replacement of mafic volcanic rock fragments and that these processes predate the extensive intergranular calcite cementation (Fig. 4B, C). The serrated edges of rock fragments support that the calcite cement postdates the early illite and chlorite formation (e.g., Fig. 4C). The late, intergranular pore-filling illite was formed after the dissolution of intergranular calcite and detrital feldspar clasts (e.g., K-feldspar) (Figs. 4E-H, 5B). Previous petrographic and modeling studies about the diagenesis of the Rotliegend sandstone also showed illite formation as a result of K-feldspar dissolution (Schöner and Gaupp, 2005; Waldmann et al., 2014; Waldmann and Gaupp, 2016). Similarly, the possible ions for late illite precipitation in the studied samples could have been derived from the partial dissolution of K-feldspar.

Depositional conditions and diagenetic evolution of the Kupferschiefer (T1)

The deposition of the T1 represents a major change in the depositional paleoenvironment, which involved the flooding of the Permian intracontinental depression and the development of the Kupferschiefer Sea (Rentzsch, 1965; Legler et al., 2005; Fig. 1B). Importantly, the availability of reduced sulfur exerts a strong control on the behavior of a number of RSTEs, which can also be used as proxies for depositional paleoenvironments (Tribovillard et al., 2006; Algeo and Liu, 2020; Bennett and Canfield, 2020). The enrichment of some RSTEs (e.g., Mo, U, V, Ni, and Cr) in the organic matter-rich lower T1 (Fig. 15) is consistent with highly reducing conditions in the bottom waters or pore fluids during sediment deposition. The behavior of Mo is particularly useful; for example, Mo enrichment in modern anoxic systems has been used to distinguish noneuxinic (nonsulfidic, <25 ppm), seasonally/intermittently euxinic (25–100 ppm), and persistently euxinic (sulfidic, i.e., H_2S-bearing, >100 ppm) conditions, respectively (Scott and Lyons, 2012). The Mo concentration of samples from the T1 reflects persistently euxinic (lower T1, Mo > 100 ppm) to seasonally euxinic (middle T1 and upper T1, Mo = 25–100 ppm) bottom water or pore water conditions (Fig. 16).

Covariation between Mo and U is sensitive to both seawater Eh and water mass connectivity (Algeo and Tribovillard, 2009; He et al., 2021). Based on the U_{EF} and Mo_{EF} relationship (Fig. 16), the T1 was deposited in anoxic (nonsulfidic) to euxinic conditions, before a transition to suboxic and then to oxic conditions during the deposition of the Ca1. Furthermore, the T1 in the Saale subbasin preserves similar U_{EF} and Mo_{EF} systematics as samples from the adjacent Thuringian subbasin (located to the southwest of the Saale subbasin) and were interpreted to have been deposited under open marine conditions (Ruebsam et al., 2017; Fig. 16). The one exception is the group of samples from the Sangerhausen, which preserve relatively lower Mo values in the lower T1 and could be related to remobilization by the oxidizing fluid that produced the Rote Fäule alteration (Fig. 15A). Though the cause for Mo but not U removal in the lower T1 from Sangerhausen is not clear here, one possible explanation is that Mo and U have different redox potentials, so it may be that the fluids were not quite oxidizing enough to mobilize U. Alternatively, the other possible explanation could be that U was locally bounded in clay-organic nanocomposites (Kennedy et al., 2014; Löhr and

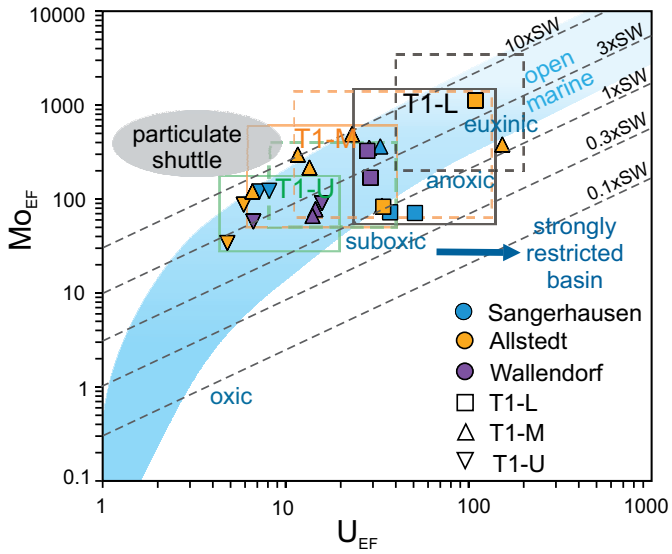

Fig. 16. A plot showing U_{EF} vs. Mo_{EF}, annotated with the different redox zones, including oxic, anoxic (ferruginous), and euxinic (H_2S-bearing). Enrichment factors (EF) for Mo and U were calculated relative to the Post-Archean Australian Shale (PAAS; Taylor and McLennan, 1985). Solid rectangles for samples from this study and dotted rectangles for samples from the Thuringian subbasin (Ruebsam et al., 2017). Colors of the rectangles: black = lower T1 (T1-L), orange = middle T1 (T1-M), and green = T1 (T1-U).

Kennedy, 2014). It may also be related to biotic processes that are the prominent driver of U reduction in organic-matter-rich sediments, and direct enzymatic U microbial reduction could increase the rate of U immobility (U^{6+} can be reduced to U^{4+} in such reactions) as evidenced in roll-front U deposits (e.g., Min et al., 2005).

Other RSTEs show relative enrichment in specific sulfide zones (e.g., Co in the Cu zone and Cd in the Zn-Pb zone; Fig. 14A-C). This probably shows either mobility of these elements by the mineralizing fluids or, more likely, the addition of these elements from the mineralizing fluids into the system. In contrast, the correlation between other RSTEs (e.g., Mo, U, V, Ni, and Cr) and total organic carbon (Fig. 15A-C) and their lack of covariation with base metals (Cu, Zn, and Pb) (Fig. 14D-G) indicate no significant mobility of these elements by the mineralizing fluids, and they can be used for paleoenvironmental interpretations (Stüeken et al., 2020).

In terms of diagenetic mineral phases, similar to the S1, textural evidence shows calcite and dolomite cements were the earliest phases in the T1. Early diagenetic carbonate cements can be formed under anoxic conditions in marine fine-grained siliciclastic sediments as a by-product of microbial sulfate reduction (Loyd and Smirnoff, 2022). However, understanding the source(s) of these fine-grained carbonate cements will require further investigations using in situ C and O isotope analyses (e.g., Denny et al., 2020; Cui et al., 2021).

Differentiating detrital and authigenic illite in the T1, especially in clay-rich fine-grained laminations, is very challenging. However, illite in carbonate-rich intervals was predominantly formed after the dissolution of carbonates (calcite and dolomite) and clasts (Fig. 9A, B). Similar to the Rotliegend sandstone, the dissolution of K-feldspar likely contributed ions to illite precipitation in the T1. Pore fluids may be another pos-

sible source of ions for illite precipitation; this cannot be ruled out from this study.

Our detailed petrographic observations showed both the sulfides and authigenic illite were formed after calcite dissolution, but the exact timing remains uncertain. Previous studies used illite crystallinity and K-Ar geochronology to discriminate between authigenic illite in mineralized and unmineralized zones. In general, illite in the mineralized zone in the Polish basin preserved lower crystallinity (Bechtel et al., 1999). The K-Ar age of the clay-size fraction (<2 µm) of the mineralized samples in this basin is ~250 Ma, whereas the age of diagenetic illite is estimated to range from 216 to 190 Ma (Bechtel et al., 1999). Furthermore, the $\delta^{18}O$ and δD values of illite in the Rote Fäule and Cu zone were used to show the interaction between illite with the mineralizing fluids (Bechtel et al., 2000). For example, the shift in $\delta^{18}O$ (decrease by ~4‰) and δD (increase by ~40‰) values of illite from the Rote Fäule to the Cu zone in the Polish basin and Richelsdorf ore district in Germany have been attributed to fluid-rock interaction with ascending, oxidizing, mineralizing fluids (Bechtel and Hoernes, 1993; Bechtel et al., 2000). These lines of evidence, together with our petrographic observation that sulfides and authigenic illite precipitated after calcite dissolution, suggest that some authigenic illite formation could at least overlap or postdate the mineralization.

Diagenetic evolution of the Zechstein limestone (Ca1)

The Ca1 shares key diagenetic features with the T1, including early diagenetic carbonate cementation, illite formation, and sulfide precipitation associated with carbonate dissolution (Fig. 10A, B). Similar to the T1, detrital quartz and feldspars are uncompacted and cemented by early diagenetic calcite cement. The calcite cement is restricted to intercrystalline pores without any precursor dolomite fabrics (e.g., Fu et al., 2008). The lack of textural evidence, meteoric diagenetic assemblages at this diagenetic stage (e.g., Al-Hashimi and Hemingway, 1973; Ronchi et al., 2004; Nader et al., 2008), and absence of local anhydrite unit at the Sangerhausen site as a Ca^{2+} fluid source (Schoenherr et al., 2018) imply dedolomitization is not the likely process for the formation of the vuggy pores in the Ca1. Dedolomitization is a slow process that can increase porosity (e.g., Lucia, 1995, 2004) or occlude porosity, depending on the presence (e.g., anhydrite dissolution) or absence of Ca^{2+}-rich fluid sources (Escorcia et al., 2013; Schoenherr et al., 2018). In a hand-specimen (cm) scale, these vuggy pores are aligned in specific directions in the lowermost samples of the Ca1 and disappear upward. Therefore, the formation of these vuggy pores is related to selective dissolution of calcite cemented dolomite grains, probably by the mineralizing fluids (Figs. 7F, 10C).

The sulfides were mostly formed after the dissolution of highly calcite cemented areas of dolomite that have vuggy pores (Fig. 10E, F). Similar to S1 and T1, illite is formed after carbonate dissolution, with cations likely sourced from dissolution of K-feldspar (Fig. 10B).

Trace element associations and timing of high-grade sulfide mineralization in the Saale subbasin

The base metal sulfides in the three units include bornite in the Cu zone and sphalerite and galena in the overlapping Zn-Pb zone (Figs. 6A-H, 8C-H, 9C-E, 10C). The base metal data also reflect the vertical metal zonation in the studied drill cores (Fig. 11A-C). Zinc (sphalerite) is more proximal to the Cu zone than Pb (galena) in the Zn-Pb zone, and this could reflect the slight difference in their solubility during sulfide precipitation (Seward and Barnes, 1997; Huston et al., 2016). The distribution of certain trace elements also reflects the zonation of the major sulfide phases. For example, trace elements such as Bi, Ag, and Sb are primarily partitioned into galena and Cd into sphalerite (Cook et al., 2009; George et al., 2015). The enrichment of Cd in the Zn-Pb zone, therefore, may reflect its partitioning into sphalerite and/or galena (Table 1; Fig. 14A). Consistent with this interpretation, trace element analysis using laser ablation (LA)-ICP-MS on sulfides from the Polish Kupferschiefer showed higher Cd concentrations in sphalerite but not in bornite and chalcopyrite (Foltyn et al., 2022).

Different timings have been proposed for the high-grade Cu and Zn-Pb mineralization in the Kupferschiefer, from early diagenetic (e.g., Wedepohl and Rentzsch, 2006) to hydrothermal mineralization induced by tectonic fracturing (Jowett, 1986, 1987; Cathles et al., 1993). Most of the early diagenetic models are based on (1) the interpretation of early pyrite replacement and low $\delta^{34}S$ values of sulfides and (2) the laterally extensive stratiform style of the mineralization, especially in the fine-grained carbonaceous mudstones of the T1 (e.g., Wedepohl and Rentzsch, 2006). Pre-ore, framboidal pyrite in the T1 and Ca1 is preserved in organic matter- and clay-rich laminations and likely formed before carbonate cementation during early diagenesis or even in the water column. In contrast, the high-grade Cu and Zn-Pb sulfides are formed mostly as a replacement of early diagenetic intergranular calcite cement in S1 and T1 (Figs. 6D, 9B-E). The lack of grain collapse following calcite dissolution is consistent with synchronous calcite dissolution-sulfide precipitation. It may also suggest that the high-grade, disseminated, sulfide mineralization occurred at relatively shallow depths, i.e., grains were partially dissolved but lithostatic pressure was insufficient to cause the skeletal grains to collapse.

The other important feature is the replacement of detrital feldspar by sulfides, which is most readily observed in the S1 (Fig. 6A-C) and coarser-grained laminations in the lower T1 (Fig. 8C-H). For example, in the S1 from Allstedt, rounded detrital K-feldspar (and intragranular calcite) has been replaced by bornite (Fig. 6A-C). In the T1, petrographic comparison between unmineralized and mineralized domains shows abundant carbonate and subordinate feldspar replacement by sulfides, whereas quartz was less affected (Fig. 8A-D). The angular shape of sulfides (e.g., bornite) replacing detrital clasts in these coarse-grained laminations also provides indirect evidence for sulfide replacement of feldspar clasts (Fig. 8E).

Overall, our preferred model involves the influx of Cu-bearing hydrothermal fluids into the S1, T1, and Ca1 following early diagenesis, which resulted in the dissolution and replacement of calcite and feldspar by sulfides (Fig. 17). It is generally accepted that the Cu-bearing fluids that formed SSC deposits had a weakly acidic to neutral pH (Wedepohl and Rentzsch, 2006; Hitzman et al., 2010; Borg et al., 2012). As there is no evidence of widespread phyllosilicate altera-

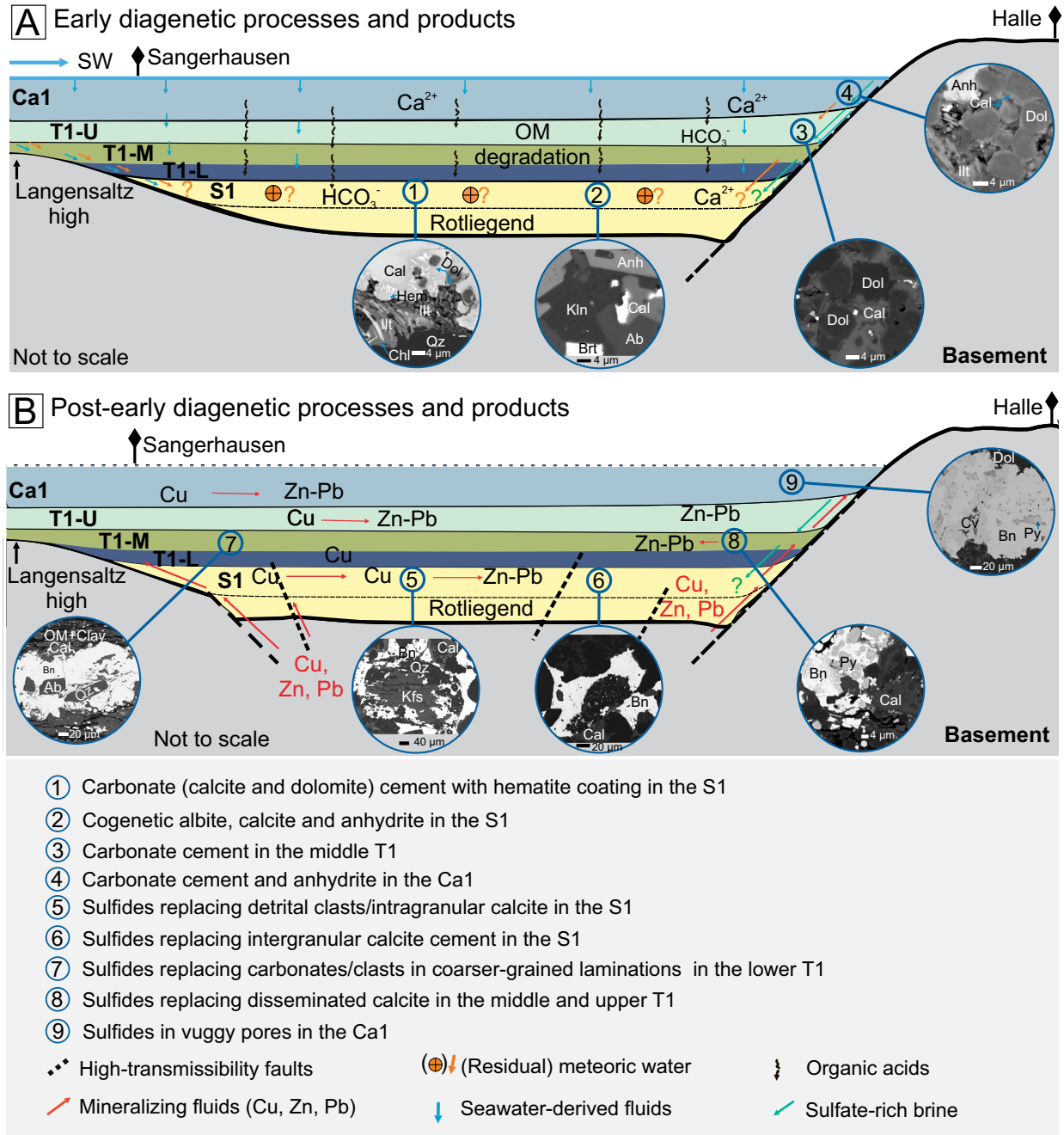

Fig. 17. Schematic diagram summarizing early (A) and postearly (B) diagenetic processes and products in the S1, T1, and Ca1. The inset backscattered electron images show the typical mineralogical assemblages in the three units during early and postearly diagenetic times. Extensive calcite cement, mostly postdating clast alteration, in the three units was formed during early diagenesis. The sulfides in this system are formed as a replacement of detrital clast (and intragranular calcite cement) in the S1 and mostly in lower T1, intergranular calcite cement in the S1 and middle and upper T1, and calcite cemented dolomite forming vuggy porosity in the Ca1. Ab = albite, Anh = anhydrite, Bn = bornite, Brt = barite, Ca1 = Zechstein limestone, Cal = calcite, Chl = chlorite, Cv = covellite, Dol = dolomite, Hem = hematite, Ilt = illite, Kln = kaolinite, OM = organic matter, Py = pyrite, Py_F = framboidal pyrite, Qz = quartz, S1 = Rotliegend sandstone, SW = seawater, T1-L = lower Kupferschiefer, T1-M = middle Kupferschiefer, T1-U = upper Kupferschiefer.

tion in the Rotliegend, therefore, the acidity that resulted in the dissolution of calcite and feldspar was likely to have been generated in situ during fluid-rock interaction and fluid mixing (e.g., Corbella et al., 2004; Zhang et al., 2021; Magnall et al., 2023).

Implications

The samples from the Saale subbasin contain fine-grained Cu and Pb-Zn sulfides that are hosted in the uppermost Rotliegend sandstone (S1), Kupferschiefer (T1), and overlying Zechstein limestone (Ca1). This stratigraphic interval records

a major change in the depositional environment that followed the Zechstein marine transgression (e.g., Legler et al., 2005; Legler and Schneider, 2008). Importantly, the diagenetic evolution of units separated by major stratigraphic boundaries can have a major influence on reservoir heterogeneities (Morad et al., 2000, 2010, 2012; Al-Ramadan et al., 2012). For example, early diagenetic processes are primarily controlled by the mineralogy of detrital phases, pore fluid chemistry, organic matter content, and residence time of sediments under specific geochemical conditions (Ketzer et al., 2003a, b; Morad et al., 2000, 2010, 2012).

In the Saale subbasin, the immature primary sediment composition and transition toward seawater-dominated pore fluid chemistry across the S1-T1 boundary were key factors controlling the diagenetic evolution of the system. In particular, the distribution of early diagenetic carbonate, which was then subsequently replaced by sulfides, was a major factor controlling the influx of metal-bearing fluids through the S1 and T1 units. Reaction permeability developed when metal-bearing mineralizing fluids reacted with calcite in the host rock, resulting in fluid migration and sulfide precipitation. This model is similar to carbonate replacement models for clastic-dominant (CD-type) Zn deposits, which are also hosted by carbonate-rich siliciclastic units (e.g., Magnall et al., 2021; Spinks et al., 2021). Future research may further elucidate the mineralizing fluid migration pathways in the host rocks by mapping the carbonate cement using techniques such as hyperspectral imaging and micro-X-ray fluorescence in cores, integrated with micro- to nanoscale imaging techniques (e.g., transmission electron microscopy) to better understand the interface reactions between sulfides and other mineral phases (e.g., Magnall et al., 2023).

Conclusions

Copper and Zn-Pb sulfide mineralized rocks in the Saale subbasin (Eastern Germany) formed primarily via the replacement of diagenetic carbonate cement in the uppermost Rotliegend (S1), Kupferschiefer (T1), and Zechstein limestone (Ca1). Early calcite cementation in the Rotliegend (S1) unit occluded high levels of precompaction primary porosity and was followed by diagenetic alteration of detrital feldspar clasts. In the overlying T1 unit, petrographic and mineralogical data show an increase in carbonate (calcite and dolomite) cement. Enrichment of RSTEs (e.g., Mo) and covariation with total organic matter in the lower T1 are consistent with the development of highly reducing depositional (euxinic) conditions. The styles of sulfide replacement in the S1 and T1 are similar, although the highest base metal grades (max. Cu = 2.4 wt %, Zn = 3.1 wt %, Pb = 1 wt %) are associated with carbonate in the middle T1. The most volumetrically important mineralization style involved the replacement of intergranular calcite cement in the S1 and in the middle and upper T1. A second style of sulfide mineralization involved the replacement of detrital feldspar clasts. In the Ca1 unit, sulfide mineralization has formed in vuggy pore spaces. Overall, the reduced nature of the T1 provided the necessary redox gradient for sulfide precipitation, and the dissolution of diagenetic carbonate was the main factor controlling reaction permeability and the lateral migration of hydrothermal fluids in the Saale subbasin.

Acknowledgments

Funding for this project was provided by the Helmholtz Recruitment Initiative grant to Sarah Gleeson. We acknowledge the Landesamt für Geologie und Bergwesen, Sachsen-Anhalt, for supplying core samples from their repository. We thank Uwe Dittmann for thin and thick section preparation, Hartmut Liep for sample powdering, Andrea Gottsche for assistance during sample preparation for XRD analysis, Ilona Schäpan for BSE imaging and EDS analysis, and Sylvia Pinkerneil for total organic carbon analysis, all at GFZ-Potsdam. We particularly acknowledge Simon Jones and Jonathan Cloutier for their thorough and thoughtful reviews of this paper.

REFERENCES

Alderton, D.H.M., Selby, D., Kucha, H., and Blundell, D.J., 2016, A multi-stage origin for Kupferschiefer mineralization: Ore Geology Reviews, v. 79, p. 535–543.

Algeo, T.J., and Liu, J., 2020, A re-assessment of elemental proxies for paleoredox analysis: Chemical Geology, v. 540, article 119549.

Algeo, T.J., and Tribovillard, N., 2009, Environmental analysis of paleoceanographic systems based on molybdenum-uranium covariation: Chemical Geology, v. 268, p. 211–225.

Al-Hashimi, W.S., and Hemingway, J.E., 1973, Recent dedolomitization and the origin of the rusty crusts of Northumberland: Journal of Sedimentary Research, v. 43, p. 82–91.

Al-Ramadan, K., Morad, S., Plink-Björklund, P., Ketzer, J.M., and De Ros, L.F., 2012, Distribution of diagenetic alterations in relationship to depositional facies and sequence stratigraphy of a wave and tide-dominated siliciclastic shoreline complex: Upper Cretaceous Chimney Rock sandstones, Wyoming and Utah, USA: International Association of Sedimentologists Special Publications, v. 45, p. 271–296.

Bechtel, A., and Hoernes, S., 1993, Stable isotopic variations of clay minerals: A key to the understanding of Kupferschiefer-type mineralization, Germany: Geochimica et Cosmochimica Acta, v. 57, p. 1799–1816.

Bechtel, A., and Püttmann, W., 1991, The origin of the Kupferschiefer-type mineralization in the Richelsdorf Hills, Germany, as deduced from stable isotope and organic geochemical studies: Chemical Geology, v. 91, p. 1–18.

Bechtel, A., Elliott, W.C., and Oszczepalski, S., 1996, Indirect age determination of Kuperfschiefer-type mineralization in the Polish basin by K/Ar dating of illite; preliminary results: Economic Geology, v. 91, p. 1310–1319.

Bechtel, A., Elliott, W.C., Wampler, J.M., and Oszczepalski, S., 1999, Clay mineralogy, crystallinity, and K-Ar ages of illites within the Polish Zechstein basin; implications for the age of Kupferschiefer mineralization: Economic Geology, v. 94, p. 261–272.

Bechtel, A., Shieh, Y.-N., Elliott, W.C., Oszczepalski, S., and Hoernes, S., 2000, Mineralogy, crystallinity and stable isotopic composition of illitic clays within the Polish Zechstein basin: Implications for the genesis of Kupferschiefer mineralization: Chemical Geology, v. 163, p. 189–205.

Bechtel, A., Sun, Y., Püttmann, W., Hoernes, S., and Hoefs, J., 2001, Isotopic evidence for multi-stage base metal enrichment in the Kupferschiefer from the Sangerhausen basin, Germany: Chemical Geology, v. 176, p. 31–49.

Bennett, W.W., and Canfield, D.E., 2020, Redox-sensitive trace metals as paleoredox proxies: A review and analysis of data from modern sediments: Earth-Science Reviews, v. 204, article 103175.

Bergmann, J., Friedel, P., and Kleeberg, R., 1998, BGMN—a new fundamental parameters based Rietveld program for laboratory X-ray sources, it's use in quantitative analysis and structure investigations: UCr Commission on Powder Diffraction Newsletter, v. 20, p. 5–8.

Böning, P., Fröllje, H., Beck, M., Schnetger, B., and Brumsack, H.-J., 2012, Underestimation of the authigenic fraction of Cu and Ni in organic-rich sediments: Marine Geology, v. 323–325, p. 24–28.

Borg, G., 2017, It's all about timing—the origin of the European Kupferschiefer ores: World of Mining—Surface and Underground, v. 69, p. 24–30.

Borg, G., Piestrzynski, A., Bachmann, G.H., Püttmann, W., Walther, S., and Fiedler, M., 2012, An overview of the European Kupferschiefer deposits: Society of Economic Geologists, Special Publication 16, p. 455–486.

Brauns, C.M., Pätzold, T., and Haack, U., 2003, A Re-Os study bearing on the age of the Kupferschiefer mineralization at Sangerhausen [abs.]:

International Congress of Carboniferous and Permian Stratigraphy, 15th, Utrecht, 2003, Abstracts, p. 66.

Breitkreuz, C., Geißler, M., Schneider, J., and Kiersnowski, H., 2008, Basin initiation: Volcanism and sedimentation, *in* Littke, R., Bayer, U., Gajewski, D., and Nelskamp, S., eds., Dynamics of complex intracontinental basins: Springer-Verlag Berlin, p. 173–180.

Cathles, L.M., Oszczepalski, S., and Jowett, E.C., 1993, Mass balance evaluation of the late diagenetic hypothesis for Kupferschiefer Cu mineralization in the Lubin basin of southwestern Poland: Economic Geology, v. 88, p. 948–956.

Cook, N.J., Ciobanu, C.L., Pring, A., Skinner, W., Shimizu, M., Danyushevsky, L., Saini-Eidukat, B., and Melcher, F., 2009, Trace and minor elements in sphalerite: A LA-ICPMS study: Geochimica et Cosmochimica Acta, v. 73, p. 4761–4791.

Corbella, M., Ayora, C., and Cardellach, E., 2004, Hydrothermal mixing, carbonate dissolution and sulfide precipitation in Mississippi Valley-type deposits: Mineralium Deposita, v. 39, p. 344–357.

Cui, H., Kitajima, K., Orland, I.J., Xiao, S., Baele, J.-M., Kaufman, A.J., Denny, A., Zhou, C., Spicuzza, M.J., and Fournelle, J.H., 2021, Deposition or diagenesis? Probing the Ediacaran Shuram excursion in South China by SIMS: Global and Planetary Change, v. 206, article 103591.

Denny, A.C., Orland, I.J., and Valley, J.W., 2020, Regionally correlated oxygen and carbon isotope zonation in diagenetic carbonates of the Bakken Formation: Chemical Geology, v. 531, article 119327.

Dickinson, W.R., 1970, Interpreting detrital modes of graywacke and arkose: Journal Sedimentary Petrology, v. 40, p. 695–707.

Dickinson, W.R., and Suczek, C.A., 1979, Plate tectonics and sandstone compositions: American Association of Petroleum Geologists, AAPG Bulletin, v. 63, p. 2164–2182.

Dickinson, W.R., Beard, L.S., Brakenridge, G.R., Erjavec, J.L., Ferguson, R.C., Inman, K.F., Knepp, R.A., Lindberg, F.A., and Ryberg, P.T., 1983, Provenance of North American Phanerozoic sandstones in relation to tectonic setting: Geological Society of America Bulletin, v. 94, p. 222–235.

Doebelin, N., and Kleeberg, R., 2015, Profex: A graphical user interface for the Rietveld refinement program BGMN: Journal of Applied Crystallography, v. 48, p. 1573–1580.

Ehling, B.-C., Gebhardt, U., and Kampe, A., 2008, Rotliegend, *in* Bachmann, G.H., Ehling, B.-C., Eichner, R., and Schwab, M., eds., Geologie von Sachsen-Anhalt: Zeitschrift zur Geschichte des Berg-und Hüttenwesens, v. 14, p. 143–160.

El-Ghali, M.A.K., Mansurbeg, H., Morad, S., Al-Aasm, I., and Ajdanlisky, G., 2006, Distribution of diagenetic alterations in fluvial and paralic deposits within sequence stratigraphic framework: Evidence from the Petrohan Terrigenous Group and the Svidol Formation, Lower Triassic, NW Bulgaria: Sedimentary Geology, v. 190, p. 299–321.

El-Ghali, M.A.K., El Khoriby, E., Mansurbeg, H., Morad, S., and Ogle, N., 2013, Distribution of carbonate cements within depositional facies and sequence stratigraphic framework of shoreface and deltaic arenites, lower Miocene, the Gulf of Suez rift, Egypt: Marine and Petroleum Geology, v. 45, p. 267–280.

Erzberger, R., Franz, R., Jung, W., Knitzschke, G., Langer, M., Luge, J., Rentzsch, H., and Rentzsch, J., 1968, Lithologie, paläogeographie und metallführung des kupferschiefers in der Deutschen Demokratischen Republik: Geologie, v. 17, p. 776–791.

Escorcia, L.C., Gomez-Rivas, E., Daniele, L., and Corbella, M., 2013, Dedolomitization and reservoir quality: Insights from reactive transport modelling: Geofluids, v. 13, p. 221–231.

Foltyn, K., Erlandsson, V.B., Zygo, W., Melcher, F., and Pieczonka, J., 2022, New perspective on trace element (Re, Ge, Ag) hosts in the Cu-Ag Kupferschiefer deposit, Poland: Insight from a LA-ICP-MS trace element study: Ore Geology Reviews, v. 143, article 104768.

Franz, R., 1965, Metallfazies und Rote Fäule im Unteren Zechstein bei Spremberg-Weißwasser, Freiberg. Forschh: Freiberger Forschungshefte, v. C193, p. 41–54.

Fu, Q., Qing, H., Bergman, K.M., and Yang, C., 2008, Dedolomitization and calcite cementation in the middle Devonian Winnipegosis Formation in central Saskatchewan, Canada: Sedimentology, v. 55, p. 1623–1642.

Gebhardt, U., and Hiete, M., 2013, Continental upper Carboniferous red beds in the Variscan intermontane Saale basin, central Germany: Orbital forcing detected by wavelet analysis: Geological Society, London, Special Publications, v. 376, p. 177–199.

Geologisches Landesamt Sachsen-Anhalt, 1993, Geologische Übersichtskarte von Sachsen-Anhalt: Halle, Germany, Geologisches Landesamt Sachsen-Anhalt, scale 1:400,000.

George, L., Cook, N.J., Ciobanu, C.L., and Wade, B.P., 2015, Trace and minor elements in galena: A reconnaissance LA-ICP-MS study: American Mineralogist, v. 100, p. 548–569.

Greenwood, P.F., Brocks, J.J., Grice, K., Schwark, L., Jaraula, C.M.B., Dick, J.M., and Evans, K.A., 2013, Organic geochemistry and mineralogy. I. Characterisation of organic matter associated with metal deposits: Ore Geology Reviews, v. 50, p. 1–27.

Grice, K., Schaeffer, P., Schwark, L., and Maxwell, J.R., 1997, Changes in palaeoenvironmental conditions during deposition of the Permian Kupferschiefer (Lower Rhine basin, northwest Germany) inferred from molecular and isotopic compositions of biomarker components: Organic Geochemistry, v. 26, p. 677–690.

He, Z., Clarkson, M.O., Andersen, M.B., Archer, C., Sweere, T.C., Kraal, P., Guthauser, A., Huang, F., and Vance, D., 2021, Temporally and spatially dynamic redox conditions on an upwelling margin: The impact on coupled sedimentary Mo and U isotope systematics, and implications for the Mo-U paleoredox proxy: Geochimica et Cosmochimica Acta, v. 309, p. 251–271.

Heppenheimer, H., Hagemann, H.W., and Püttmann, W., 1995, A comparative study of the influence of organic matter on metal accumulation processes in the Kupferschiefer from the Hessian depression and the North Sudetic syncline: Ore Geology Reviews, v. 9, p. 391–409.

Hitzman, M.W., Selley, D., and Bull, S., 2010, Formation of sedimentary rock-hosted stratiform copper deposits through Earth history: Economic Geology, v. 105, p. 627–639.

Huston, D.L., Mernagh, T.P., Hagemann, S.G., Doublier, M.P., Fiorentini, M., Champion, D.C., Jaques, A.L., Czarnota, K., Cayley, R., and Skirrow, R., 2016, Tectono-metallogenic systems—the place of mineral systems within tectonic evolution, with an emphasis on Australian examples: Ore Geology Reviews, v. 76, p. 168–210.

Jowett, E.C., 1986, Genesis of Kupferschiefer Cu-Ag deposits by convective flow of Rotliegendes brines during Triassic rifting: Economic Geology, v. 81, p. 1823–1837.

——1987, Formation of sulfide-calcite veinlets in the Kupferschiefer Cu-Ag deposits in Poland by natural hydrofracturing during basin subsidence: The Journal of Geology, v. 95, p. 513–526.

Jowett, E.C., Pearce, G.W., and Rydzewski, A., 1987, A Mid-Triassic paleomagnetic age of the Kupferschiefer mineralization in Poland, based on a revised apparent polar wander path for Europe and Russia: Journal of Geophysical Research: Solid Earth, v. 92, p. 581–598.

Jung, W., and Knitzschke, G., 1976, Kupferschiefer in the German Democratic Republic (GDR) with special reference to the Kupferschiefer deposit in the southeastern Harz foreland, *in* Wolf, K.H., ed., Handbook of stratabound and stratiform ore deposits: Amsterdam, Elsevier, p. 353–406.

Kennedy, M.J., Löhr, S.C., Fraser, S.A., and Baruch, E.T., 2014, Direct evidence for organic carbon preservation as clay-organic nanocomposites in a Devonian black shale; from deposition to diagenesis: Earth and Planetary Science Letters, v. 388, p. 59–70.

Ketris, M., and Yudovich, Y.E., 2009, Estimations of Clarkes for Carbonaceous biolithes: World averages for trace element contents in black shales and coals: International Journal of Coal Geology, v. 78, p. 135–148.

Ketzer, J.M., Morad, S., Evans, R., and Al-Aasm, I.S., 2002, Distribution of diagenetic alterations in fluvial, deltaic, and shallow marine sandstones within a sequence stratigraphic framework: Evidence from the Mullaghmore Formation (Carboniferous), NW Ireland: Journal of Sedimentary Research, v. 72, p. 760–774.

Ketzer, J.M., Morad, S., and Amorosi, A., 2003a, Predictive diagenetic clay-mineral distribution in siliciclastic rocks within a sequence stratigraphic framework: International Association of Sedimentologists, Special Publication 34, p. 43–61.

Ketzer, J.M., Holz, M., Morad, S., and Al-Aasm, I.S., 2003b, Sequence stratigraphic distribution of diagenetic alterations in coal-bearing, paralic sandstones: Evidence from the Rio Bonito Formation (early Permian), southern Brazil: Sedimentology, v. 50, p. 855–877.

Kulick, J., Leifeld, D., Meisl, S., Pöschl, W., Stellmacher, R., and Strecker, G., 1984, Petrofazielle und chemische Erkundung des Kupferschiefers der Hessischen Senke und des Harz-Westrandes: Geologisches Jahrbuch. Reihe D. Mineralogie, Petrographie, Geochemie, Lagerstättenkunde, v. D68, p. 3–223.

Lanson, B., Beaufort, D., Berger, G., Bauer, A., Cassagnabere, A., and Meunier, A., 2002, Authigenic kaolin and illitic minerals during burial diagenesis of sandstones: A review: Clay Minerals, v. 37, p. 1–22.

Legler, B., and Schneider, J.W., 2008, Marine ingressions into the middle/late Permian saline lake of the Southern Permian basin (Rotliegend, Northern

Germany) possibly linked to sea-level highstands in the Arctic rift system: Palaeogeography, Palaeoclimatology, Palaeoecology, v. 267, p. 102–114.

Legler, B., Gebhardt, U., and Schneider, J.W., 2005, Late Permian non-marine–marine transitional profiles in the central Southern Permian basin, northern Germany: International Journal of Earth Sciences, v. 94, p. 851–862.

Little, S.H., Vance, D., Lyons, T.W., and McManus, J., 2015, Controls on trace metal authigenic enrichment in reducing sediments: insights from modern oxygen-deficient settings: American Journal of Science, v. 315, p. 77–119.

Löhr, S.C., and Kennedy, M.J., 2014, Organomineral nanocomposite carbon burial during Oceanic Anoxic Event 2: Biogeosciences, v. 11, p. 4971–4983.

Loyd, S.J., and Smirnoff, M.N., 2022, Progressive formation of authigenic carbonate with depth in siliciclastic marine sediments including substantial formation in sediments experiencing methanogenesis: Chemical Geology, v. 594, article 120775.

Lucia, F.J., 1995, Rock-fabric/petrophysical classification of carbonate pore space for reservoir characterization: American Association of Petroleum Geologists, AAPG Bulletin, v. 79, p. 1275–1300.

——2004, Origin and petrophysics of dolostone pore space: Geological Society, London, Special Publications, v. 235, p. 141–155.

Magnall, J.M., Gleeson, S.A., Poulton, S.W., Gordon, G.W., and Paradis, S., 2018, Links between seawater paleoredox and the formation of sediment-hosted massive sulphide (SHMS) deposits—Fe speciation and Mo isotope constraints from Late Devonian mudstones: Chemical Geology, v. 490, p. 45–60.

Magnall, J.M., Hayward, N., Gleeson, S.A., Schleicher, A., Dalrymple, I., King, R., and Mahlstadt, N., 2021, The Teena Zn-Pb deposit (McArthur basin, Australia). Part II: Carbonate replacement sulfide mineralization during burial diagenesis—implications for mineral exploration: Economic Geology, v. 116, p. 1769–1801.

Magnall, J.M., Wirth, R., Hayward, N., Gleeson, S.A., and Schreiber, A., 2023, Stratiform host-rock replacement via self-sustaining reactions in a clastic-dominated (CD-type) Zn deposit: Economic Geology, v. 118, p. 823–836, doi: 10.5382/econgeo.4988.

Maystrenko, Y., Bayer, U., Brink, H.-J., and Littke, R., 2008, The Central European basin system—an overview, *in* Littke, R., Bayer, U., Gajewski, D., and Nelskamp, S., eds., Dynamics of complex intracontinental basins—the Central European basin system: Berlin, Springer-Verlag, p. 17–34.

Menning, M., Alekseev, A.S., Chuvashov, B.I., Davydov, V.I., Devuyst, F.-X., Forke, H.C., Grunt, T.A., Hance, L., Heckel, P.H., and Izokh, N.G., 2006, Global time scale and regional stratigraphic reference scales of central and west Europe, east Europe, Tethys, south China, and North America as used in the Devonian-Carboniferous-Permian Correlation Chart 2003 (DCP 2003): Palaeogeography, Palaeoclimatology, Palaeoecology, v. 240, p. 318–372.

Min, M., Xu, H., Chen, J., and Fayek, M., 2005, Evidence of uranium biomineralization in sandstone-hosted roll-front uranium deposits, northwestern China: Ore Geology Reviews, v. 26, p. 198–206.

Mohammedyasin, M.S., Magnall, J.M., Gleeson, S.A., Schulz, H.-M., Schleicher, A.M., Stammeier, J.A., and Ehling, B.-C., 2022, Quantitative mineralogy and bulk rock geochemistry of the Kupferschiefer system, Saale subbasin, Eastern Germany: GFZ Data Services, doi: 10.5880/GFZ.3.1.2022.006.

Morad, S., Bergan, M., Knarud, R., and Nystuen, J.P., 1990, Albitization of detrital plagioclase in Triassic reservoir sandstones from the Snorre field, Norwegian North Sea: Journal of Sedimentary Research, v. 60, p. 411–425.

Morad, S., Ketzer, J.M., and De Ros, L.F., 2000, Spatial and temporal distribution of diagenetic alterations in siliciclastic rocks: Implications for mass transfer in sedimentary basins: Sedimentology, v. 47, p. 95–120.

Morad, S., Al-Ramadan, K., Ketzer, J.M., and De Ros, L.F., 2010, The impact of diagenesis on the heterogeneity of sandstone reservoirs: A review of the role of depositional facies and sequence stratigraphy: American Associaton of Petroleum Geologists, AAPG Bulletin, v. 94, p. 1267–1309.

Morad, S., Ketzer, J.M., and De Ros, L.F., 2012, Linking diagenesis to sequence stratigraphy: An integrated tool for understanding and predicting reservoir quality distribution: International Association of Sedimentologists Special Publications, v. 45, p. 1–36.

Nader, F.H., Swennen, R., and Keppens, E., 2008, Calcitization/dedolomitization of Jurassic dolostones (Lebanon): Results from petrographic and sequential geochemical analyses: Sedimentology, v. 55, p. 1467–1485.

Oszczepalski, S., 1989, Kupferschiefer in southwestern Poland: Sedimentary environments, metal zoning, and ore controls: Geological Association of Canada, Special Paper 36, p. 571–600.

Oszczepalski, S., Speczik, S., Zieliński, K., and Chmielewski, A., 2019, The Kupferschiefer deposits and prospects in SW Poland: Past, present and future: Minerals, v. 9, p. 1–42.

Pašava, J., Oszczepalski, S., and Du, A., 2010, Re-Os age of non-mineralized black shale from the Kupferschiefer, Poland, and implications for metal enrichment: Mineralium Deposita, v. 45, p. 189–199.

Paul, J., 2006, Der Kupferschiefer: Lithologie, stratigraphie, fazies und metallogenese eines schwarzschiefers: Zeitschrift der Deutschen Gesellschaft für Geowissenschaften, v. 157, p. 57–76.

Pharaoh, T., Dusar, M., Geluk, M., Kockel, F., Krawczyk, C., Krzywiec, P., Scheck-Wenderoth, M., Thybo, H., Vejbæk, O., and van Wees, J.D., 2010, Chapter 3: Tectonic evolution, in Doornenbal, H. and Stevenson, A. eds., Petroleum geological atlas of the Southern Permian basin area: Houten, The Netherlands, European Association of Geoscientists and Engineers (EAGE), p. 25–57.

Pieczonka, J., Piestrzyński, A., Mucha, J., Głuszek, A., Kotarba, M.J., and Więcław, D., 2008, The red-bed-type precious metal deposit in the Sieroszowice-Polkowice copper mining district, SW Poland: Annales Societatis Geologorum Poloniae, v. 78, p. 151–280.

Piestrzyński, A., Pieczonka, J., and Głuszek, A., 2002, Redbed-type gold mineralisation, Kupferschiefer, south-west Poland: Mineralium Deposita, v. 37, p. 512–528.

Plein, E., 1990, The southern Permian basin and its paleogeography, *in* Heling, D., Rothe, P., Förstner, U., and Stoffers, P., eds., Sediments and environmental geochemistry: Berlin, Springer-Verlag, p. 124–133.

Poetz, S., Liu, Y., Magnall, J.M., Vieth-Hillebrand, A., Yang, S., Göthel, M., Gleeson, S.A., and Schulz, H.-M., 2022, Signals of low grade organic matter alteration in the upper Permian Kupferschiefer (Spremberg area, Eastern Germany)—a by-product of copper mineralization?: Organic Geochemistry, v. 169, article 104421.

Rahfeld, A., Kleeberg, R., Möckel, R., and Gutzmer, J., 2018, Quantitative mineralogical analysis of European Kupferschiefer ore: Minerals Engineering, v. 115, p. 21–32.

Reinhard, C.T., Planavsky, N.J., Wang, X., Fischer, W.W., Johnson, T.M., and Lyons, T.W., 2014, The isotopic composition of authigenic chromium in anoxic marine sediments: A case study from the Cariaco basin: Earth and Planetary Science Letters, v. 407, p. 9–18.

Rentzsch, J., 1965, Die feinstratigraphisch-lithologische Flözparallelisierung im Kupferschiefer am Südrand des norddeutschen Zechsteinbeckens: Die Zeitschrift für Angewandte Geologie, v. 11, p. 11–14.

Ronchi, P., Jadoul, F., and Savino, R., 2004, Quaternary dedolomitization along fracture systems in a Late Triassic dolomitized platform (western southern Alps, Italy): Carbonates and Evaporites, v. 19, p. 51–66.

Ruebsam, W., Dickson, A.J., Hoyer, E.-M., and Schwark, L., 2017, Multiproxy reconstruction of oceanographic conditions in the southern epeiric Kupferschiefer Sea (late Permian) based on redox-sensitive trace elements, molybdenum isotopes and biomarkers: Gondwana Research, v. 44, p. 205–218.

Rydzewski, A., 1978, Oxidative facies of the Zechstein copper-bearing shale in the Fore-Sudetic monocline: Przeglad Geologiczny, v. 26, p. 102–107.

Sawlowicz, Z., 1989, On the origin of copper mineralization in the Kupferschiefer: A sulphur isotope study: Terra Nova, v. 1, p. 339–343.

Schneider, J., and Romer, R.L., 2010, The late Variscan molasses (late Carboniferous to late Permian) of the Saxo-Thuringian zone, *in* Linnemann, U., and Rommer, R.L., eds., Pre-Mesozoic geology of Saxo-Thuringia: From the Cadomian active margin to the Variscan orogen: Stuttgart, Schweizerbart, p. 323–346.

Schneider, J.W., Rößler, R., and Gaitzsch, B., 1995, Proposal for a combined reference section of the Central European Continental Carboniferous and Permian for correlations with marine standard sections: Permophiles, v. 26, p. 26–31.

Schoenherr, J., Reuning, L., Hallenberger, M., Lüders, V., Lemmens, L., Biehl, B.C., Lewin, A., Leupold, M., Wimmers, K., and Strohmenger, C.J., 2018, Dedolomitization: Review and case study of uncommon mesogenetic formation conditions: Earth-Science Reviews, v. 185, p. 780–805.

Schöner, R., and Gaupp, R., 2005, Contrasting red bed diagenesis: The southern and northern margin of the Central European basin: International Journal of Earth Sciences, v. 94, p. 897–916.

Scott, C., and Lyons, T.W., 2012, Contrasting molybdenum cycling and isotopic properties in euxinic versus non-euxinic sediments and sedimentary rocks: Refining the paleoproxies: Chemical Geology, v. 324, p. 19–27.

Seward, T.M., and Barnes, H.L., 1997, Metal transport by hydrothermal ore fluids, *in* Barnes, H.L., ed., Geochemistry of hydrothermal ore deposits: New York, Wiley, p. 435–486.
Slack, J.F., McAleer, R.J., Shanks, W.C., III, and Dumoulin, J.A., 2021, Diagenetic barite-pyrite-wurtzite formation and redox signatures in Triassic mudstone, Brooks Range, northern Alaska: Chemical Geology, v. 585, article 120568.
Smith, D.B., 1979, Rapid marine transgressions and regressions of the upper Permian Zechstein Sea: Journal of the Geological Society, v. 136, p. 155–156.
Spinks, S.C., Pearce, M.A., Liu, W., Kunzmann, M., Ryan, C.G., Moorhead, G.F., Kirkham, R., Blaikie, T., Sheldon, H.A., Schaubs, P.M., and Rickard, W.D.A., 2021, Carbonate replacement as the principal ore formation process in the Proterozoic McArthur River (HYC) sediment-hosted Zn-Pb deposit, Australia: Economic Geology, v. 116, p. 693–718.
Stollhofen, H., Bachmann, G.H., Barnasch, J., Bayer, U., Beutler, G., Franz, M., Kästner, M., Legler, B., Mutterlose, J., and Radies, D., 2008, Upper Rotliegend to Early Cretaceous basin development, *in* Littke, R., Bayer, U., Gajewski, D., and Nelskamp, S., eds., Dynamics of complex intracontinental basins: Berlin, Heidelberg, Springer-Verlag, p. 181–210.
Stüeken, E.E., Jones, S., Raub, T.D., Prave, A.R., Rose, C.V, Linnekogel, S., and Cloutier, J., 2020, Geochemical fingerprints of seawater in the late Mesoproterozoic Midcontinent rift, North America: Life at the marine-land divide: Chemical Geology, v. 553, article 119812.
Sullivan, M.D., Haszeldine, R.S., Boyce, A.J., Rogers, G., and Fallick, A.E., 1994, Late anhydrite cements mark basin inversion: Isotopic and formation water evidence, Rotliegend sandstone, North Sea: Marine and Petroleum Geology, v. 11, p. 46-54.
Sun, Y.-Z., and Püttmann, W., 1997, Metal accumulation during and after deposition of the Kupferschiefer from the Sangerhausen basin, Germany: Applied Geochemistry, v. 12, p. 577–592.
——2000, The role of organic matter during copper enrichment in Kupferschiefer from the Sangerhausen basin, Germany: Organic Geochemistry, v. 31, p. 1143–1161.
Symons, D.T.A., Kawasaki, K., Walther, S., and Borg, G., 2011, Paleomagnetism of the Cu-Zn-Pb–bearing Kupferschiefer black shale (upper Permian) at Sangerhausen, Germany: Mineralium Deposita, v. 46, p. 137–152.
Taylor, S.R., and McLennan, S.M., 1985, The continental crust: Its composition and evolution: Oxford, Blackwell, 312 p.
Tribovillard, N., Algeo, T. J., Lyons, T., and Riboulleau, A., 2006, Trace metals as paleoredox and paleoproductivity proxies: An update: Chemical Geology, v. 232, p. 12–32.
Ulmer-Scholle, D.S., Scholle, P.A., Schieber, J., and Raine, R.J., 2015, Grains: Rock fragments (lithic fragments): American Association of Petroleum Geologists, Memoir 109, p. 39–78.
Wagner, T., and Lorenz, J., 2002, Mineralogy of complex Co-Ni-Bi vein mineralization, Bieber deposit, Spessart, Germany: Mineralogical Magazine, v. 66, p. 385–407.
Waldmann, S., and Gaupp, R., 2016, Grain-rimming kaolinite in Permian Rotliegend reservoir rocks: Sedimentary Geology, v. 335, p. 17–33.
Waldmann, S., Busch, A., Van Ojik, K., and Gaupp, R., 2014, Importance of mineral surface areas in Rotliegend sandstones for modeling CO_2-water-rock interactions: Chemical Geology, v. 378, p. 89–109.
Wedepohl, K.H., 1971, Kupferschiefer as a prototype of syngenetic sedimentary ore deposits: Japan Society for Mineralogy and Geology, v. 3, p. 268–273.
Wedepohl, K.H., and Rentzsch, J., 2006, The composition of brines in the early diagenetic mineralization of the Permian Kupferschiefer in Germany: Contributions to Mineralogy and Petrology, v. 152, p. 323–333.
Wedepohl, K.H., Delevaux, M.H., and Doe, B.R., 1978, The potential source of lead in the Permian Kupferschiefer bed of Europe and some selected Paleozoic mineral deposits in the Federal Republic of Germany: Contributions to Mineralogy and Petrology, v. 65, p. 273–281.
Wilkinson, J.J., Vowles, K., Muxworthy, A.R., and MacNiocaill, C., 2017, Regional remagnetization of Irish Carboniferous carbonates dates Variscan orogenesis, not Zn-Pb mineralization: Geology, v. 45, p. 747–750.
Wilson, M., Neumann, E.-R., Davies, G.R., Timmerman, M.J., Heeremans, M., and Larsen, B.T., 2004, Permo-Carboniferous magmatism and rifting in Europe: Introduction: Geological Society, London, Special Publications, v. 223, p. 1–10.
Worden, R.H., and Morad, S., 2003, Clay minerals in sandstones: Controls on formation, distribution and evolution, *in* Worden, R.H., and Morad, S., eds., Clay mineral cements in sandstones: International Association of Sedimentologists, Special Publication 34, p. 3–41.
Worden, R.H., Morrall, G.T., Kelly, S., McArdle, P., and Barshep, D.V., 2020, A renewed look at calcite cement in marine-deltaic sandstones: The Brent Reservoir, Heather Field, northern North Sea, UK: Geological Society, London, Special Publications, v. 484, p. 305–335.
Zhang, Y., Li, W., Cai, Y., Qu, Y., Pan, Y., Zhang, W., and Zhao, K., 2021, Experimental investigation of the reactions between pyrite and aqueous Cu (I) chloride solution at 100–250°C: Geochimica et Cosmochimica Acta, v. 298, p. 1–20.
Ziegler, P., 1990, Geological atlas of western and central Europe: Bath, Shell International Petroleum Maatschappij B.V., Geological Society Publishing House, 239 p.
Zientek, M.L., Oszczepalski, S., Parks, H.L., Bliss, J.D., Borg, G., Box, S.E., Denning, P., Hayes, T.S., Spieth, V., and Taylor, C.D., 2015, Assessment of undiscovered copper resources associated with the Permian Kupferschiefer, Southern Permian basin, Europe: U.S. Geological Survey, Scientific Investigations Report 2010-5090-U, 94 p.

Mohammed Seid Mohammedyasin is currently a Ph.D. student at GFZ Helmholtz Centre Potsdam and Free University Berlin, Germany. He completed his B.Sc. degree in applied geology at Arba Minch University (Ethiopia) and M.Sc. degrees in petroleum geoscience and mineral exploration geology at Norwegian University of Science and Technology and Addis Ababa University (Ethiopia). Mo's Ph.D. project is investigating the diagenetic and hydrothermal processes involved in the formation of sediment-hosted stratiform Cu deposits in the Kupferschiefer district (Saale subbasin, Eastern Germany). Mo's research interests focus on understanding fluid-rock interactions and fluid flow pathways in the formation of sediment-hosted mineral deposits.